Optical Characterization of a Magnetostrictive Microcantilever based Sensor

Beatriz Maria Machado Silveira
Integrated Master's in Physics Engineering
Department of Physics and Astronomy
2017

Supervisor
Orlando José dos Reis Frazão, Invited Assistant Professor
Faculty of Sciences of the University of Porto and INESC TEC

Co-supervisor
André Miguel Trindade Pereira, Invited Professor
Faculty of Sciences of the University of Porto and IFIMUP IN

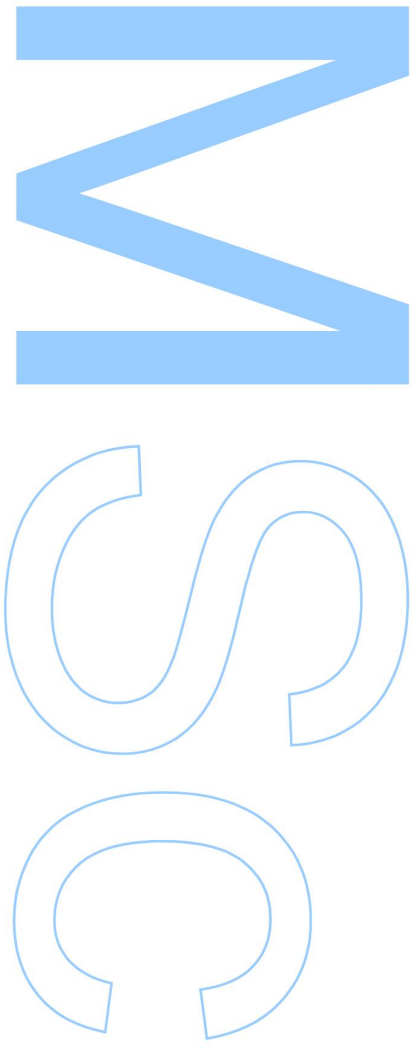

U.PORTO

FACULDADE DE CIÊNCIAS
UNIVERSIDADE DO PORTO

Todas as correções determinadas pelo júri, e só essas, foram efetuadas.

O Presidente do Júri,

Porto, _____/_____/_____

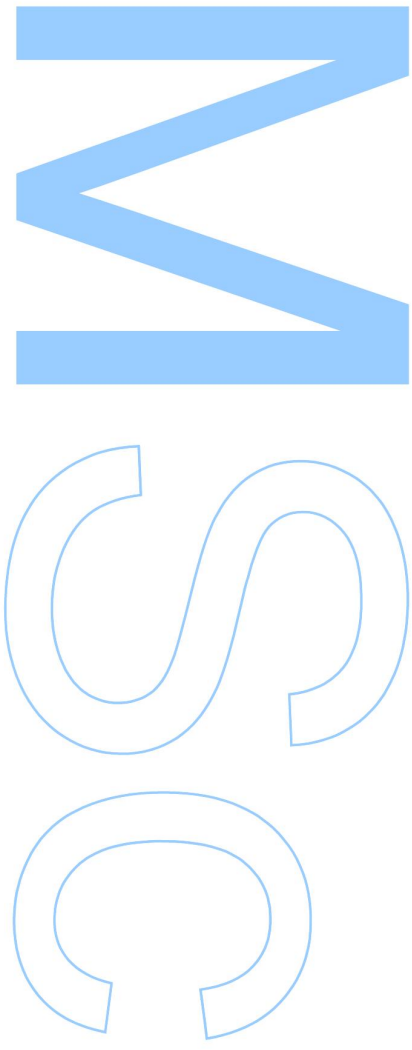

Acknowledgements

The work developed during these past months was certainly not accomplished individually. For that reason, I'd like to express my gratitude to the many people involved and who made this Master's dissertation possible.

First of all, I would like to thank my supervisor and mentor, Dr. Orlando Frazão, for all his guidance, support and feedback, but more important for sharing his ideas and time with me. I would also like to thank him for helping me widen my scientific knowledge and improve my academic record. To my co-supervisor, Dr. André Pereira, I am grateful for his dedication and encouragement, which was always welcome and almost always needed. To both, I am thankful for the vote of confidence and for giving me the opportunity of working with new people in different environments.

I would like to thank INESC-TEC and all the professors and investigators that I met along the way. Particularly, I would like to thank my colleagues André and Ricardo, whom I truly look up to, for all the insight, discussions, suggestions and valuable help.

To IPHT, I would like to thank for welcoming me so warmly. It was a pleasure to work with such dedicated people during my short stay in Germany. I would especially like to thank Dr. Hartmut Bartelt, Dr. Manfred Rothhardt, Dr. Martin Becker, Dr. Jan Dellith, Tina Eschrich, and Tobias Tieβ.

I would like to acknowledge IFIMUP-IN and all my colleagues in the lower floor. To João Horta and Ana Pires, for making their valuable time available for me, a big thank you. Their determination and persistence inspired me to work harder. To Inês Figueiredo, I would like to thank for teaching me how to use the big machines, and to Tiago Ferreira, for providing useful data for this work.

I want to thank João Pedro Conde and Virgínia Chu for receiving me so welcomingly in INESC-MN. A special thank you to Rui Pinto, for being so patient and for teaching me so much about microfabrication in just a week.

My most sincere thank you to my family, for always supporting me and believing in me. To my parents, brother and sister I dedicate this Master's thesis.

Lastly, to my great friends, my dear Paul, Joana, Kiko, Granja, Pedro, Jorge, Páramos, João, Rui, Gonçalo, Luís, and Duarte. This Master's is the end of a chapter, so thank you for being there along the way.

Abstract

This Master's dissertation explores the development of an optical system to detect deflection on a micrometric scale, in structures magnetically actuated. In ferromagnetic materials, the magnetic moments align with an external magnetic field. This process leads to a change in the length of the material in the direction of the magnetic moments. This effect, known as magnetostriction, is present in all ferromagnetic materials and their alloys. By depositing a thin layer of a magnetostrictive material on the surface of a microcantilever, a deflection of its free end is expected when an external magnetic field is applied.

In this dissertation, an optical characterization system to measure microcantilever deflection was assembled. The measuring system is comprised of two main components: a taper tip and a magnetostrictive microcantilever. Magnetostrictive thin films were deposited using EBPVD and characterized using XRD, VSM, and SQUID. Microfabrication techniques, such as Magnetron Sputtering Deposition, PECVD, and Reactive Ion Etching, were used to fabricate a die of microcantilevers, above which a magnetostrictive layer was later deposited. The optical tapers were produced from conventional $SMF28e$ optical fibers using CO_2 laser ablation, and Vyctran and Ring of Fire technologies. The taper tips were produced by cleaving the tapers and milling a polished flat-top surface using FIB technology. The measuring system uses a taper tip to shine light on a microcantilever. The light beam is reflected in the glass-air interface of the taper tip and again in the microcantilever. The microcantilever displacement under a magnetic field is measured by analyzing the reflected light spectrum. This measuring system based on Fabry-Perot interferometry allowed for the measuring of deflections of $0.25\mu m$ in a magnetic field range from $0Oe$ to $70Oe$. Additionally, two structures were produced in taper tips using FIB milling, to overcome instability issues found in the previous system.

The results obtained during this work are discussed and compared for different characterization systems, and future work ideas are proposed.

Resumo

Esta dissertação de Mestrado explora o desenvolvimento de um sistema ótico para detetar deflexões a nível micrométrico em estruturas magneticamente atuadas. Em materiais ferromagnéticos, os momentos magnéticos alinham-se segundo um campo magnético externo, induzindo uma variação no comprimento do material na direção do campo aplicado. Este efeito, conhecido como magnetostrição, está presente em todos os materiais ferromagnéticos. Depositando um filme fino magnetostritivo na superfície de um microcantilever, é esperada a deflexão da sua extremidade livre na presença de um campo magnético.

Nesta dissertação foi desenvolvido um sistema de caracterização ótico para medir deflexão em microcantileveres. O sistema de medida é composto por duas componentes principais: uma ponta taper e um microcantilever magnetostritivo. Foram depositados filmes magnetostritivos através de *EBPVD*, e foi feita a sua caracterização através de *XRD, VSM* e *SQUID*. Técnicas de fabricação, como *Magnetron Sputtering*, *PECVD* e *Reactive Ion Etching*, foram usadas para fabricar uma matriz de microcantilevers, sobre a qual foi posteriormente depositada uma camada de $Co_{66}Fe_{34}$, material magnetostrivo. Os tapers óticos foram produzidos a partir de fibra ótica convencional $SMF28e$, através de ablação com laser de CO_2 e das tecnologias Vyctran e Ring of Fire. As pontas tapers foram produzidas clivando os tapers óticos e polindo a sua superfície usando a tecnologia *FIB*. O sistema de medição usa uma ponta taper para fazer incidir um feixe de luz num microcantilever. O feixe de luz é refletido na superfície da ponta taper e no microcantilever. A deflexão do microcantilever é medida através da análise do espetro de reflexão da luz. Este sistema de medição baseado em interferometria de Fabry-Perot permitiu medir deflexões de $0.25\mu m$ numa gama de campo magnético até $70Oe$. Duas estruturas foram ainda produzidas em pontas taper usando *FIB* para colmatar instabilidades no sistema anterior.

Os resultados obtidos são discutidos e comparados para diferentes sistemas de caracterização, e ideias de trabalho futuro são propostas.

Contents

List of Figures

List of Tables

Nomenclature

Variables

Q-factor	Quality factor
ω	resonance angular frequency
κ	stiffness
m	mass; magnetic moment
ε	effective magnetostriction
ε_S	saturation magnetostrictive coefficient
l	length
Δl	elongation
t	thickness
E	Young modulus
υ	Poisson coefficient
d_{33}	strain coefficient
D	displacement
M	molecular mass; magnetization
B	magnetic field
H	magnetic field intensity
V	mass per square centimeter and per second; volume; voltage
P	pressure
Q	photocurrent
I	current
T	temperature
R	signal magnitude
φ	phase
d_{hkl}	interplanar distance

θ	angle
λ	wavelength
r	radius
n	refractive index
L	cavity length

Indices

$(\cdot)_f$	thin film
$(\cdot)_s$	substrate
$(\cdot)_S$	saturation
$(\cdot)_r$	remanence; reflected
$(\cdot)_c$	coercive; critical
$(\cdot)_i$	incident
$(\cdot)_t$	transmitted
$(\cdot)_\parallel$	longitudinal
$(\cdot)_\perp$	orthogonal
$(\cdot)_0$	equilibrium; initial
$(\cdot)_{pp}$	peak-to-peak

Units and Unit Multiples

ppm	parts per million
$wt\%$	weight percentage
s	second
min	minute
K	Kelvin
$^\circ C$	Celsius
Pa	Pascal
bar	Bar

m	meter
A	ampere
V	Volt
eV	electron Volt
W	Watt
T	Tesla
Oe	Oersted
$^{\circ}$	degree
Hz	Hertz
dB	decibel
m	mili
μ	micro
n	nano
$\mathring{A}$	Angstrom
p	pico

Abbreviations

AC	Alternate Current
AFM	Atomic Force Microscopy
bcc	body-centered cubic
BSE	Backscattered Electrons
CCD	Charge-Coupled Device
CEMUP-MNTEC	Centro de Materiais da Universidade do Porto - Micro e Nano Fabricação
DC	Direct Current
DI	Deionized
EBPVD	Electron Beam Physical Vapor Deposition
EDS	Energy-Dispersive X-Ray Spectroscopy
fcc	face-centered cubic
FIB	Focused Ion Beam
FP	Fabry-Perot

FSR	Free Spectral Range
IFIMUP-IN	Instituto de Física dos Materiais da Universidade do Porto
INESC-MN	Instituto de Engenharia de Sistemas e Computadores - Microsistemas e Nanotecnologias
INESC-TEC	Instituto de Engenharia de Sistemas e Computadores - Tecnologia e Ciência
IPA	Isopropanol
LabVIEW	Laboratory Virtual Instrument Engineering Workbench
laser	Light Amplification by Stimulated Emission of Radiation
LDS	Large Diameter Splicer
MEMS	Microelectromechanical Systems
MSMC	Magnetostrictive Microcantilevers
OPD	Optical Path Difference
OSA	Optical Spectrum Analyzer
PECVD	Plasma Enhanced Chemical Vapor Deposition
PSD	Position Sensitive Detector
PZT	Piezoelectric
RF	Radio Frequency
RIE	Reactive Ion Etching
SE	Secondary Electron
SEM	Scanning Electron Microscope
SMF	Single Mode Fiber
SQUID	Superconducting Quantum Interference Device
TEM	Transmission Electron Microscope
VSM	Vibrating Sample Magnetometer
XRD	X-Ray Diffraction

Chapter I

Preface

1.1 Motivation

Fiber-optic sensors have been attracting great attention in the past few years due to their outstanding advantages, such as compact size and design, immunity to electromagnetic interference, and low cost [2]. In telecommunications, the need for faster and lossless transmission media lead to an increasing investigation around optical fibers. In medical applications, optical fibers are being used for non-invasive investigation or surgical procedures due to their biocompatibility. The implementation of fiber-optical sensors in microelectromechanical systems, MEMS, allows the production of new devices which can be remotely actuated and activated, and can be incorporated in critical environments. [3]. Particularly, magnetostrictive materials are increasingly being introduced in MEMS as actuators, sensors, and vibration devices [4], specifically in the form of magnetostrictive microcantilevers, MSMC. Their high sensitivity and performance are valuable qualities for the implementation of MSMCs in biosensors [5]. MSMCs are wireless and easily addressed using magnetic fields [6]. Moreover, magnetostrictive microcantilevers present much higher Q-factors both in air and liquid, compared with other cantilevers [7]. This fact might come as an advantage, especially when the sensor is to be implemented in biological media.

The combination of optical fibers with nanotechnology allowed the gradual reduction of the core and cladding of the optical fiber to micrometric dimensions, creating the taper. Tapered optical fibers have recently attracted considerable attention for a wide variety of biological, photonics, and engineering applications [8, 9, 10]. Tapered fibers present unique optical guidance characteristics, such as low loss, fast response, tight confinement, and strong evanescent field, highly appreciated in industry. Besides, tapered fibers are more flexible than traditional optical fibers, reducing the size of the sensor [8].

In this dissertation, a system to measure deflection in magnetostrictive microcantilevers will be explored. The goal is to assemble an optical characterization system to measure micrometric displacements under an applied magnetic field. This dissertation is divided into seven chapters. In Chapter I, the motivation behind this work is presented. The chapter also includes a section where the main goals of the work are described. In Chapter II, the state of the art, the advances in the different areas addressed in this work are synthesized, particularly deflection measuring systems using microcantilevers, the magnetostrictive effect, and optical fiber taper based sensors.

Chapter III describes the working principle of many microfabrication techniques used to produce a die of microcantilevers, and the deposition technique used for the layering of the magnetostriction composite on the surface of the microcantilevers. The chapter also includes a description of three taper fabrication methods and a technique to polish flat-top taper tips. Lastly, the working principle of two optical characterization systems to measure deflection in microcantilevers is discussed.

The experimental component is presented in Chapter IV. This chapter is divided into three sections. In the first section, the deposition of a magnetostrictive $Co_{66}Fe_{34}$ thin film in an amorphous silicon sample is reported and the magnetic and structural analysis of the film is presented. The second section details the fabrication of the die of microcantilevers using the microfabrication techniques introduced in the previous Chapter III. In the third section, a system to measure microcantilever displacement through an indirect method already found in literature is addressed. This method uses a laser and a Position Sensitive Detector to measure deflection in the microcantilevers, based on the position of a reflected light beam.

In Chapter V, the viability of using taper tips for the characterization of microcantilevers is evaluated, using a novel technique based on Fabry-Perot interferometry. Also in this chapter, the whole process behind taper tips fabrication using CO_2 laser ablation and FIB milling is explained.

In Chapter VI, two new structures to measure deflection are studied. Both were already fabricated using focused ion beam milling. These structures might be used in the future to correct some instabilities found in the previous optical characterization system.

Lastly, Chapter VII will include a discussion on the work developed during this dissertation, and some remarks about the future work will be made.

1.2 Objectives

The main goal of this Master's degree is to assemble a new optical characterization system to directly measure microcantilever displacement. Therefore, smaller objectives were proposed to achieve the desired result:

- fabrication of a die of magnetostrictive microcantilevers;
- study of three different techniques to create optical tapers, and a technique for polishing taper tips;
- assembly of an optical characterization system incorporating the already fabricated die of microcantilevers and the taper tips;
- investigation of the viability of using different structures milled in taper tips to measure microcantilever displacement.

1.3 Outputs

A. D. Gomes, B. Silveira, S. C. Warren-Smith, M. Becker, M. Rothhardt, and O. Frazão, "Fiber Bragg Grating on Abrupt Tapered Tip for Temperature Independent Refractive Index Measurement", IEEE Sensors Journal, 2017 (Submitted)

A. D. Gomes, B. Silveira, S. C. Warren-Smith, M. Becker, M. Rothhardt, and O. Frazão, "Fiber Bragg Grating on Abrupt Taper End for Temperature Independent Refractive Index Sensing", In III International Conference on Applications of Optics and Photonics (AOP2017), Faro, Portugal, May 2017

B. Silveira, J. H. Belo, R. Pinto, O. Frazão, V. Chu, J. P. Conde, and A. M. Pereira, "Deflection Sensor based on Magnetostrictive Microcantilevers magnetically actuated", In Symposium on Engineering Physics – 2nd Doctoral Congress in Engineering, Faculty of Engineering, University of Porto, Portugal, 8th and 9th May 2017

B. Silveira, J. H. Belo, R. Pinto, O. Frazão, V. Chu, J. P. Conde, and A. M. Pereira, "Optical Characterization of a Magnetostrictive Microcantilever based Sensor", In Jornadas de Engenharia Física, Física e Astronomia, University of Porto, Portugal, 24th March 2017

A. D. Gomes, B. Silveira, S. C. Warren-Smith, M. Becker, M. Rothhardt, and O. Frazão, "Fiber Bragg Grating on Abrupt Tapered Tip for Refractive Index and Temperature Sensing", In XIII Symposium on Enabling Optical Networks and Sensors (SEONS 2016), Universidade da Beira Interior, Covilhã, Portugal, 8th July 2016

Chapter II

State of the Art

Since their fabrication in the '80s, optical fiber tapers found numerous applications in science and technology. In this work, yet another sensing application is proposed, by combining optical tapers and magnetostrictive microcantilevers.

This chapter reports the advances in fiber-optic magnetic sensors. In particular, measuring systems to quantify deflection in microcantilevers using remotely addressed magnetostrictive sensors will be explored.

2.1 Microcantilever

Microcantilevers are structures commonly found in MEMS. Their application started in the 1980s, but it was only in the last two decades that their use was spread to almost every branch of science.

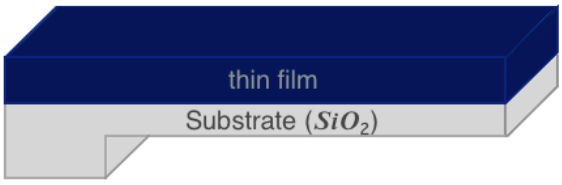

Figure 2.1: Schematic of a cantilever.

The micrometric dimensions of a microcantilever allow them to be highly portable, needing almost no packaging. Microcantilever based sensors are easily actuated and present high performance, sensitivity, and quick response [11].

2.1.1 Applications

In physics and mechanics, microcantilevers found numerous sensing applications, such detecting changes in viscosity [12], density [13], flow rate [14], stress [15], temperature [16] and humidity [17]. They can also be used to measure magnetic fields [18] and radiation pressure [19]. Moreover, microcantilevers constitute the main component in Atomic Force Microscopy, AFM, namely the probe tip [20]. Additionally, in chemistry and environmental sciences, microcantilevers are used to control the number of particles in a gas or in a liquid medium [21, 22].

More recently, microcantilevers are being arranged in arrays for incorporation in biochips and used as sensors in medicine and biology. The main advantage of using cantilever arrays as biosensors comes from the capability of monitoring different targets simultaneously [6]. In medicine, it is possible to measure, wirelessly and *in-situ*, the number of protein cells [23], cancerous cells [24, 25, 26] and viruses [27, 28, 29], leading to faster diagnosis of diseases or mutations.

2.1.2 Detection Methods

A microcantilever is comprised of a fixed and a loose end. On the cantilever, thin films with numerous characteristics can be deposited, granting different purposes to the sensor. In medicine, the thin films are usually coatings of a particular bio-recognition element, highly specific to the target species [6]. In the presence of a particular biomolecule, the receptors connect to them, increasing the mass sensed by the microcantilever [17]. This change in mass can be measured through a shift in resonance frequency of the microcantilever. In a first approximation, the mechanical resonance angular frequency, ω, of the microcantilever is given by:

$$\omega = \sqrt{\frac{k}{m}}, \tag{1}$$

where k and m are the stiffness and mass of the microcantilever, respectively.

There are various methods currently being used to measure the shift in resonance frequency and thus detect deflection on a microcantilever. One of the simplest relies on a piezoresistive material embedded on the surface of a microcantilever. In this method, when the microcantilever deflects, a strain is applied to the piezoresistive material, and the induced change in the electrical resistance can be measured by electronic means [30].

Another method is based on a capacitive measurement, where a microcantilever replaces the upper plate of a capacitor. Due to the presence of an external element in the dielectric medium, there is a change in the capacitance of the system. However, this method is not suitable for measuring large displacements, since the upper plate could come into contact with the bottom electrode, increasing the risk of damaging the cantilever [11].

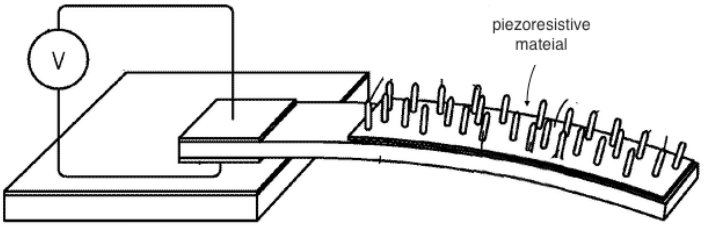

(a) Schematic of the piezoresistive method; adapted from Wang and Lao patent, 2009.

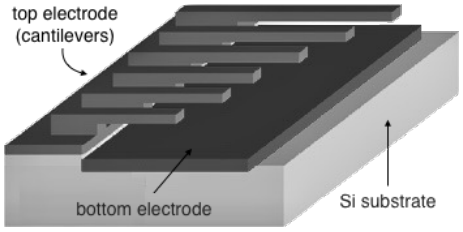

(b) Schematic of the capacitance method for multiple cantilevers.

Figure 2.2: Schematic for both piezoresistive and capacitance methods of detection.

There are two other methods for measuring deflection of cantilevers by optical means, which appear to be good candidates to be used instead of both piezoresistive and capacitive methods. The first one involves the projection of a laser beam onto the surface of the microcantilever, which is then reflected on a Position Sensitive Detector, PSD [31]. Although the laser can induce an increase in temperature and complications in the alignment of the setup, this method is more precise than the above techniques, reaching sub-nanometric resolution. The second method comprises a cleaved optical fiber kept close to the free end of the microcantilever. This technique is based on the interference of two reflected beams: one on the cleaved fiber tip and the other on the cantilever. The resulting signal is then collected by a photodiode or a spectrum analyzer [32].

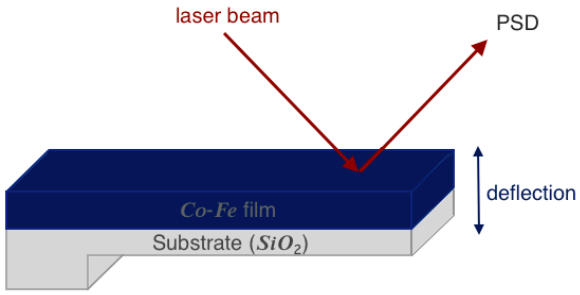

Figure 2.3: Schematic of the optical detection method using a PSD.

2.2 Magnetostriction

Magnetostriction is an inherent property of ferromagnetic materials and their alloys [33]. A ferromagnetic material is divided into regions, each one having a uniform direction of magnetization – magnetic domains. In the presence of an external magnetic field, the magnetic moments align with the direction of that field. As a result, the domain-walls move and the magnetic domains rotate towards the direction of the applied field, in order to minimize the energy of the system. This effect, known as *magnetostriction*, leads to a change in the length of the material.

Magnetostrictive materials also experience the inverse effect, known as *inverse magnetostrictive effect* or *Villari effect*. In this case, a change in the magnetic state of the magnetostrictive material occurs, under the influence of an external mechanical stress. For instance, a change in magnetization or magnetic susceptibility is observed (for a given magnetic field) when stress is applied [34].

Magnetostrictive sensors found various scientific and engineering applications over the years, including the detection of wave dispersion in ferromagnetic materials, long-range inspection of structures, and monitoring sensors in vehicle safety systems on the event of a crash [35]. Although the utilization of bulk magnetostrictive materials is increasing in sensing applications, the potential of magnetostrictive thin films is still largely unexplored.

For a sample comprised of a substrate with a deposition of a magnetostrictive film on its surface, the fractional change in length of the magnetostrictive material is given by:

$$\varepsilon = \frac{\Delta l}{l}, \tag{2}$$

where l is the initial length and Δl is the elongation. ε is a strain, not one obtained due to

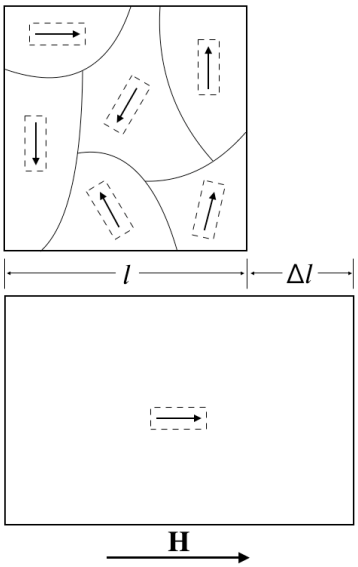

Figure 2.4: Schematic of the magnetostrictive effect, with resulting Δl elongation of the material.

an applied mechanical stress, but through a magnetic stress [36], known as *effective magnetostriction*. In this dissertation, the magnetostrictive coefficient will not be represented by λ, as it is in the literature, to avoid confusion with wavelength. The value of magnetostriction at magnetic saturation is given by the *saturation magnetostrictive coefficient*:

$$\varepsilon_S = \frac{2\left(D_{\parallel} - D_{\perp}\right) E_s t_s^2 \left(1 + \upsilon_f\right)}{9 E_f t_f l^2 \left(1 + \upsilon_s\right)}, \tag{3}$$

where l and t are the length and thickness of the magnetostrictive material, respectively, E is the Young modulus, and υ the Poisson coefficient. s and f denote the substrate and the thin film, respectively. $D_{\parallel}$ and $D_{\perp}$ represent the displacement measurements when the magnetic field is applied in a direction longitudinal and transverse to the substrate [37]. Despite being present in all pure substances, the magnetostrictive coefficient is very low, and even for strong magnetic materials, the value of ε_s is of the order of 10^{-5}, or 10 parts per million (*ppm*) [36].

2.2.1 Magnetostrictive Thin Film Materials

As mentioned above, magnetostriction is a characteristic predominantly exhibited by ferromagnetic materials and ferromagnetic based alloys. The largest magnetostriction reported in bulk form is found in rare-earth Fe alloys, in particular $Tb_x Dy_{1-x} Fe_2$, better known as *Terfenol-D*. Polycrystalline thin films of the same family also present the highest

magnetostrictive effect. The magnetostrictive coefficient was above $1000\,ppm$, and about $2600\,ppm$ for $Tb_{0.3}Dy_{0.7}Fe_2$ at saturation. Although *Terfenol-D* presents giant magnetostriction, these materials saturate only for fields $H > 0.1\,T$, restricting their use in some practical applications [37].

An alternative solution is the implementation of *Metglas* composites. For example, depositing the amorphous alloy *Metglas 2605SC* ($Fe_{81}Si_{3.5}B_{13.5}C_2$) by RF magnetron sputtering on glass and silicon substrates, a magnetostrictive coefficient of $32.0 \pm 7.7\,ppm$ was achieved [3].

More recent studies on Ga_xFe_{1-x} and $Ga_xFe_{1-x-y}Al_y$ composites show a magnetostrictive coefficient above $300\,ppm$ for an applied magnetic field in the [100] crystallographic direction of the sample [38].

2.2.2 Cobalt-Iron Alloys

Although the above-mentioned composites present high and promising magnetostrictive values, some of their chemical elements are far from abundant when compared to other magnetostrictive materials. This translates to high costs, which constitutes a drawback to their production and research in practical applications.

At room temperature, cobalt exhibits the highest saturation magnetostrictive coefficient among pure elements. Opposed to polycrystalline iron, Fe-rich alloys exhibit a large positive saturation magnetostriction [39]. For sensing applications, magnetostrictive based sensors should combine both high magnetostriction and soft magnetic properties, such as low coercivity, for which $Co-Fe$ alloys make good candidates. Studies conducted by Cooke *et al.* show that coercivity depends on many factors, such as annealing, composition and stoichiometry of the sample, and the substrate [40]. Particularly, a reduction in coercivity was observed in cases for which the samples were annealed between $375\,^{\circ}C$ and $450\,^{\circ}C$. Annealing can also increase magnetostriction in thin films, being that three times higher saturation magnetostriction coefficients where measured in annealed $Co - Fe$ samples, compared to the as-deposited samples [4, 37]. Cooke *et al.* proposed that the reason behind the significant increase in magnetostriction, when a sample is subjected to high temperatures, is related to a reduction in the sample stress due to recrystallization, increase in the grain size, and texture variations, which in turn facilitate domain rotation under a magnetic field.

Hunter *et al.* [37] measured magnetostriction at room temperature for Si/SiO_2 mi-

crocantilevers, with a deposition of magnetostrictive $Co_{1-x}Fe_x$ thin films quenched from 800 $^\circ C$. Once the cantilevers were exposed to an external magnetic field, the elongation of the magnetostrictive material forced the Si/SiO_2 arrays to bend downwards. The maximum magnetostriction reported by the authors was $260 \pm 10\, ppm$ for an annealed $Co_{66}Fe_{34}$ film. This value was three times bigger than the value for the thin film without annealing. For the same sample, the saturation magnetostriction obtained was higher than $1000\, ppm$.

Nakajima *et al.* [4] also investigated the effect of annealing in the properties of magnetostrictive $Co-Fe$ alloys. For a $Co_{68}Fe_{32}$–sputtered thin film quenched from 400 $^\circ C$, the saturation magnetostriction obtained was about $56\, ppm$, while with increasing annealing temperature up to 800 $^\circ C$, the value obtained was $159\, ppm$. The $Co_{68}Fe_{32}$ thin films were annealed for one hour and quenched in ice water.

2.3 Taper Structure

A taper is an optical fiber whose diameter is reduced by a technique of simultaneously heating and stretching the fiber, resulting in a narrow waist region and two transition regions – the down taper region and the up taper region.

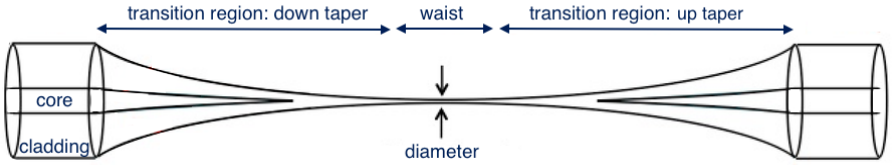

Figure 2.5: Schematic of a tapered optical fiber.

The working principle of a tapered optical fiber is based on the evanescent field interactions in the cladding-air interface. In the untapered region of the fiber, almost all light is confined within the core. However, in the transition region, the refractive indexes of the core and cladding become closer as the taper is narrowed down. As a result, the evanescent field spreads out into the cladding and reaches the external environment [41].

The first reported tapered optical fibers were fabricated from conventional optical fibers in 1981, by B. Kawasaki *et al.* [42]. Tapered optical fibers are extremely flexible due to their small diameter and present fast response, electromagnetic compatibility, low optical loss, tight confinement and large evanescent fields [8]. These properties allow taper configuration to be implemented in a wide range of applications, from temperature, curvature, strain or refractive index sensors [43, 9, 10, 44, 45], to interferometers or resonators [45, 46]. Tapers

found many applications in chemical and biological sensors, since strong evanescent fields and tight optical confinement result in increasing sensitivities of fiber-optic sensors [47].

For the characterization of microcantilevers based on the interferometric optical method mentioned above, an optical fiber tip is used to shine light on a cantilever and collect the light reflected by it. Due to the reduced dimensions of the microcantilevers used, tapered fiber tips are used in the measurements instead of optical fibers, so that less light is scattered in the reflection. Using tapers, also makes it easier to align the sensor with the microcantilevers. The techniques used to fabricate the tapers are described later on in this dissertation.

Chapter III

Fabrication and Characterization Techniques

In this chapter, the main techniques used for the fabrication and characterization of the developed sensors are described. The chapter is divided into four sections. The first two describe the deposition techniques used in the fabrication of a die of microcantilevers and methods to evaluate the resulting sample in terms of structure and magnetic properties. The third section accounts for the process of fabricating and polishing of a taper tip. Lastly, two experimental methods for measuring deflection in microcantilevers are described in the fourth section.

3.1 Deposition Techniques

3.1.1 Magnetron Sputtering Deposition

Sputter deposition is a Physical Vapor Deposition process used to grow thin films. The process consists in the ejection – sputtering – of atoms from a target, which then condensate on a substrate. In this process, a plasma is created in a vacuum chamber by ionizing an inert gas inside it, such as Ar. The plasma is comprised of Ar neutral atoms, positively charged Ar ions and electrons. When an electron collides with an Ar atom, an Ar^+ cation and 2 electrons are formed. The electrons continue to collide with Ar atoms in the plasma converting them to Ar ions. The Ar ions are accelerated by an electric field, in the direction of a negatively charged target, the material one wants to deposit [48]. For energies above the binding energies of the target atoms, the atoms can be dislodged from the target in a typical preferential direction, coating a substrate and the chamber walls.

The deposition rate depends on a large variety of parameters, such as ion gas energy and velocity, electric field intensity, pressure, and temperature inside the chamber. This

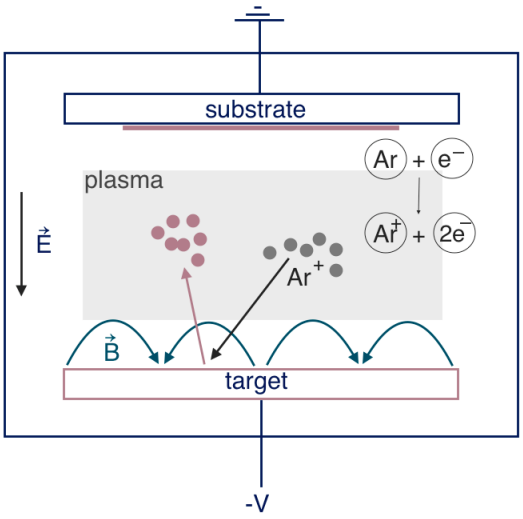

Figure 3.6: Schematic of a magnetron sputtering deposition process. Positively charged ions collide with a target species, sputtering atoms from its surface. The atoms condensate coating a substrate.

process can be limited to low ionization efficiencies of the plasma and a low deposition rate. Nevertheless, these drawbacks can be overcome by magnetron sputtering. Magnetron sputtering deposition uses magnetrons that generate closed magnetic fields to confine electrons near the surface of the target species. The electrons follow paths around the magnetic fields near the target, enhancing both the efficiency of the ionization process, and consequently the deposition rate [48].

In this work, a *Nordiko 7000* Magnetron Sputtering System was used for the depositing of an approximately $1.02\mu m$ thick *Al* layer, one of the steps leading to the fabrication of a die of microcantilevers. This layer was sputtered on a $0.7mm$ thick *Corning Glass 1737* substrate.

3.1.2 Plasma Enhanced Chemical Vapor Deposition

Chemical vapor deposition – CVD – is a process of chemically reacting a volatile compound of a material to be deposited with a gas mixture. From the reaction, the gas mixture dissociates into reactive radicals and other by-products, such as ions, neutral atoms and molecules. These precursors diffuse inside the chamber in the direction of the substrate where they are adsorbed. In the surface of the substrate, the adsorbed atoms diffuse and get organized in a thin film. There is also desorption of the volatile by-products resulting from surface reactions, which are then exhausted through an outlet, leaving the chamber

[49].

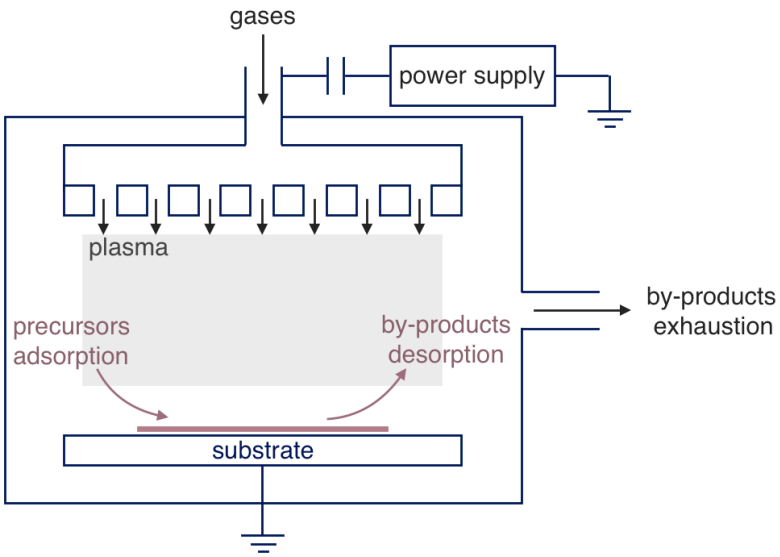

Figure 3.7: Schematic of a plasma enhanced chemical vapor deposition process. A reaction between a gas mixture and a plasma result in the adsorption of atoms in a substrate.

In plasma enhanced chemical vapor deposition – PECVD – a plasma is generated to enhance the chemical reaction rates of the precursors [49]. The plasma is usually generated by a radio frequency – RF – power supply, or by a DC discharge between two electrodes in the presence of the reacting gases. PECVD deposits uniform thin films with a good adhesion to the substrate. Moreover, since lower temperatures are achieved, this technique allows for the deposition of organic coatings.

During the fabrication of a die of microcantilevers, PECVD was used to deposit a hydrogenated amorphous silicon layer on the already patterned Al layer. The layer was approximately $0.85\mu m$ thick and made up the microcantilever structure.

3.1.3 Reactive Ion Etching

Reactive ion etching – RIE – is a type of dry etching that combines both physical and chemical etching. This process is used to remove material deposited on a substrate or wafer, in the presence of a reactive plasma. Etching is commonly performed in samples which were previously masked by a patterning process.

In a vacuum chamber, a plasma is typically generated by activating a mixture of gases with an RF power supply. The plasma consisted of a mixture of reactive species, positive ions, and electrons. The reactive species are chosen for their ability to react chemically with

the material being etched. The reactive species interact chemically with the material in the substrate, creating volatile particles that are released from the surface. Simultaneously, an electric field is used to accelerate the free electrons in the direction of the wafer, which deposit and build up negative charge around the wafer. Due to their higher mass, the positive ions almost don't move in the presence of the electric field. However, the negative build up charge around the wafer attract the positive ions, which bombard the wafer causing atoms to be sputtered [50]. This process significantly enhances the effectiveness of the chemical reaction and provides directionality to the etch. The sputtered atoms and volatile particles are removed from the chamber through an outlet.

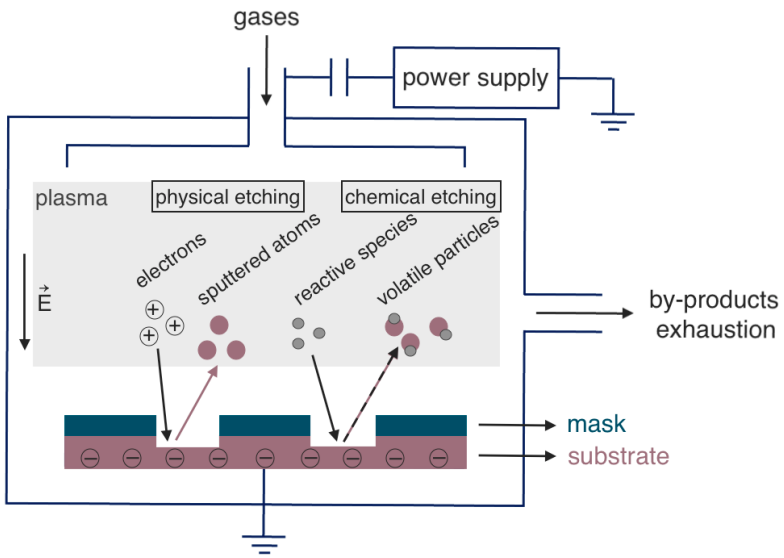

Figure 3.8: Schematic of a reactive ion etching process. Atoms in a sample are removed by both chemical and physical processes.

A major advantage to RIE is that the process can be designed to be highly anisotropic, allowing to achieve much higher resolutions and higher aspect ratios.

RIE was used to pattern the hydrogenated amorphous silicon layer, in order to form the microcantilever structure.

3.1.4 Electron Beam Physical Vapor Deposition

Electron beam physical vapor deposition, EBPVD, or e-beam evaporation, is a kind of physical vapor deposition, which is characterized as a deposition process where a solid state material undergoes a vapor phase, and then returns to a solid state thin film. E-beam evaporation is used to deposit thin films by evaporating a target material on a

substrate.

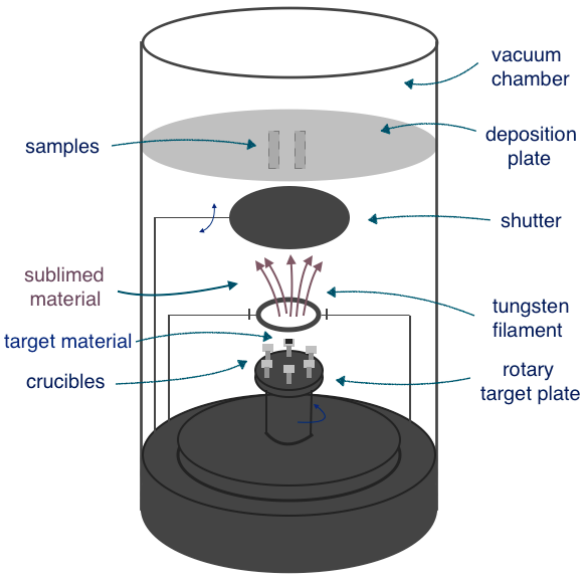

Figure 3.9: Schematic of an e-beam evaporation chamber and evaporation process.

Figure 3.9 depicts a schematic of a chamber where e-beam evaporation takes places. The electron beam can be produced using different techniques, such as thermionic emission or field electron emission. The former was the method used during this dissertation, in which a tungsten filament was heated up and an electron beam was generated. In some configurations, a magnetic field is used to guide the electron beam towards a target. The target is comprised of the material to be deposited, and is placed inside a copper crucible, usually water cooled. When the electrons collide with the target, their kinetic energy is converted into thermal energy which is transferred to the target material. When temperature and vacuum levels are sufficiently high, the target sublimates forming a vapor cloud, the shutter is opened, and the substrate is coated. The pressure inside the chamber should be at least in the order of $10^{-4} mbar$, to assure that the mean free path of the electrons is longer than the distance between the filament and the target.

It is possible to deposit more than one compound by placing different targets in more than one crucible. In the illustrated case presented in Figure 3.9, the required stoichiometry might not be achieved since there is only one filament heating up all the crucibles, and different targets evaporate at different rates. Alternatively, two filaments can generate two electron beams and direct them towards different targets through a magnetic field. By controlling the acceleration of the two beams, it is possible to modify the rate at which each target evaporates. Another possibility is to evaporate a target which is already a

compound with the desired stoichiometry [51]. The rate of evaporation is given by the Langmuir equation for evaporation,

$$V = 4.4 \times 10^{-4} \times P_0 \left(\frac{M}{T}\right)^{\frac{1}{2}}, \tag{4}$$

where V is the mass of the evaporated target material in grams per square centimeter and per second (g/cm^2s), P_0 is the equilibrium pressure, in pascal (Pa), of the sublimed material at a given temperature T, in kelvin (K), and M is the molecular mass of the material [51].

This deposition method can be used for coating with organic compounds or compounds with special physical properties (e.g. optical, electric, and magnetic), and it allows for a highly homogeneous coating thickness across the substrate.

An *Edwards Auto 306* evaporator was used to deposit a magnetostrictive thin film on a hydrogenated amorphous silicon layer, which comprised the microcantilever. The deposited material was an approximately $136nm$ thick $Co_{66}Fe_{34}$ film, whose stoichiometry was chosen for its highest magnetostrictive effect.

3.2 Thin Film Characterization Techniques

3.2.1 Scanning Electron Microscope

A scanning electron microscope, SEM, is a nanometric-resolution microscope that uses electrons to scan the surface of a sample, giving information about surface topography, crystalline structure, and chemical composition. This diversified information is only possible due to the various interactions between the electron beam and the atoms in the sample [Figure 3.10a].

In electron microscopy, the electrons in the beam can be accelerated to high energies between 2 and $1000keV$, and magnifications up to $1\,000\,000\times$ can be achieved with a $1nm$ resolution [52]. When compared to electron microscopy, optical microscopy allows for a much lower magnification, around $1000\times$, and its resolution is limited by the wavelength of visible light used in the imaging. In comparison to a transmission electron microscope, TEM, the sample preparation for SEM takes less time. To form an image in TEM the sample should be transparent to the electron beam, so its thickness usually rounds $100nm$. Moreover, in TEM, the diameter of a sample is limited to $3mm$, which corresponds to a standard TEM grid size. SEM allows for the imaging of larger specimen, being $200mm$

the limiting wafer diameter for standard SEM.

In a typical SEM, an electron beam is produced by passing a high current through a tungsten filament, which heats up emitting electrons from its tip. The produced beam is then accelerated, reaching energies between 2 and $40keV$. The beam is then focused using one or two condenser lenses, and a pair of scanning coils deflect the beam in the x and y directions, so that an area of the sample is scanned in a raster. The electron beam penetrates the specimen with a spot size of about $0.4nm$ to $5nm$, and the electrons interact with a sample in a teardrop-shaped volume, whose overall dimension depends on the electron beam energy, the atomic mass of each sample element, and the angle of the incident beam. This interaction volume extends from about $100nm$ from the surface to $5\mu m$ deep into the sample, and it's caused by absorption and scattering of the electrons that penetrate the sample. Specialized detectors allow for the imaging of the interaction between the electrons and the atoms in the sample, being that the connotation of each type of electron depends on the interaction [Figure 3.10b] [52].

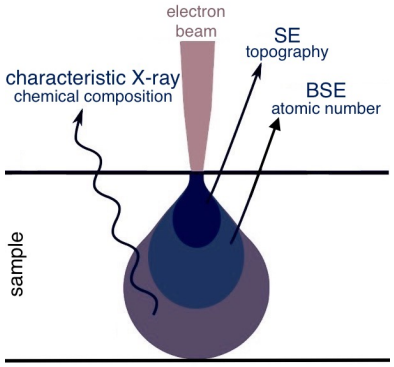

(a) Schematic of the interaction volume between the incident electron beam and the sample.

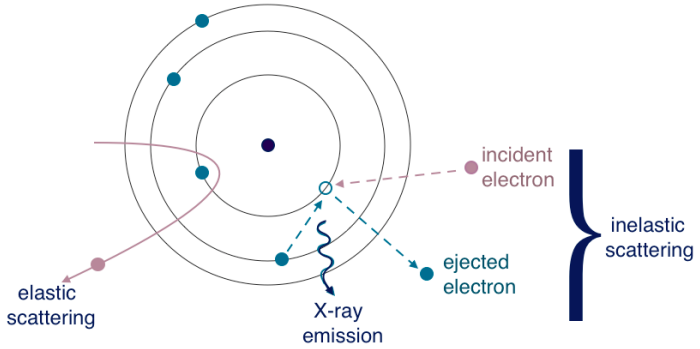

(b) Interaction mechanisms of emission of secondary electrons, backscattered electrons, and characteristic X-rays for an atom in the sample.

Figure 3.10: Effects behind SEM.

Secondary Electrons – SE

The incident electron beam – primary beam – can eject other electrons in their orbits around the atoms, by a process called inelastic scattering. The ejected electrons – secondary electrons, SE – have low energy ($< 50eV$), but give the highest resolution images about the topography of the sample, since the scattering occurs in its surface. Moreover, angled surfaces allow for more electrons to be ejected. Therefore, brighter imaging areas are usually associated with steeper or rougher regions in the surface of the sample. Since the detector of secondary electrons can also detect backscattered electrons, some compositional contrast can be detected. The imaging resolution using SE can reach $0.5nm$.

Backscattered Electrons – BSE

When primary electrons penetrate the specimen and pass through the atoms, the electrons can be elastically scattered while passing very close to the nuclei. The electrons – backscattered electrons, BSE – reemerge from the surface and are detected by a different electron detector. Elements with higher atomic number scatter electrons more strongly than elements with low atomic number. For this reason, regions with different chemical composition are recorded by the detector as a change in contrast: heavier elements appear brighter. Therefore, BSE give compositional information about a sample.

Since backscattered electrons do not collide with matter, their energy is higher than that of secondary electrons. This type of detection does not present such a high resolution when compared to SE detection, since the interaction region between the electron beam and the atoms occurs deeper in the sample.

Characteristic X-Rays

When high-energy primary electrons penetrate deeper in the sample, ejection of inner-shell electrons in the atoms of the sample can occur. To minimize energy in the atom, an outer-shell electron decays to occupy the vacancy left by the ejected electron. This decay causes the emission of an X-ray, which is detected by a photodetector. The emitted X-ray has an energy that corresponds to the energy difference between the two energy levels. The energy of the X-ray, or its wavelength, can then be related to a particular chemical component using the database for a specific element transition. This method is called energy-dispersive X-ray spectroscopy – EDS.

A *Lyra3 XMU* FIB-SEM (focused ion beam - scanning electron microscope) dual system by *Tescan* was used for the preparation of optical tapers. In this system, an ion beam

was used to mill optical fibers, while an electron beam, from an SEM column, allowed for a simultaneous high resolution imaging of the milling process.

3.2.2 X-Ray Diffraction

X-Ray crystallography is a technique used to obtain information regarding structure and stress of crystalline materials. This technique is based on the diffraction of an X-ray beam inside a crystal described by Bragg's Law of diffraction, specifically the Bragg condition. The production of X-rays is typically done in an X-ray tube, or Crooke's tube. A heated filament, usually tungsten, generates an electron beam by thermionic emission, which is then accelerated by a high electric potential. The accelerated electrons collide with a metal plate, typically copper, and *brehmsstrahlung* – braking radiation – X-rays are produced when the electrons are decelerated upon collision. When the beam electrons have sufficient energy upon collision with the metal plate, inner-shell electrons can be ejected from the metal atoms. Outer-shell electrons can then occupy the vacancy left, emitting x-ray photons with specific energies determined by the electron energy levels – characteristic X-rays [52]. The X-ray beam is then filtered to a single wavelength and collimated before being focused on the crystal.

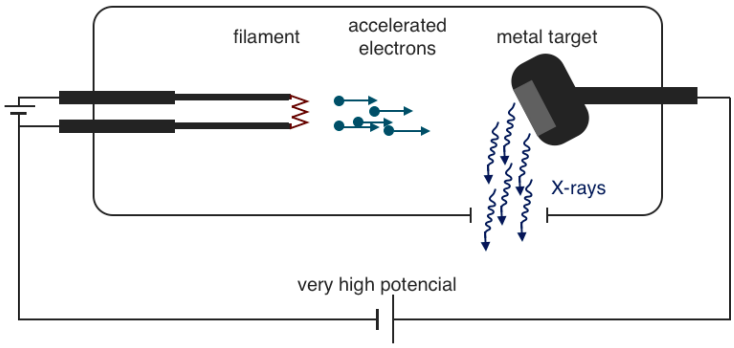

Figure 3.11: Schematic of X-ray production.

When radiation is incident on a crystal, with a propagation wavelength of the same order as the interplanar distance of the crystal, radiation is scattered by the atoms in the lattice planes. The scattered beams interfere constructively and destructively producing a diffraction pattern on a detector. When the difference in optical path of the scattered beams is an integer multiple of the radiation wavelength, constructive interference takes place, and a Bragg peak appears in the diffraction pattern – Bragg condition.

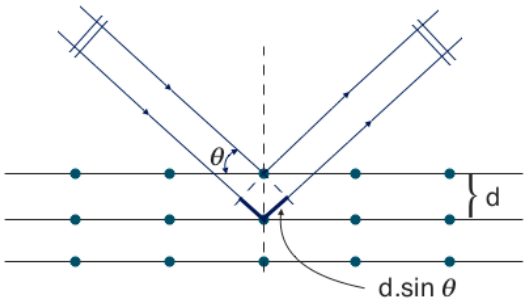

Figure 3.12: Schematic of X-ray diffraction on an crystal lattice.

Geometrically, the optical path difference – OPD – between diffracted beams is given by $OPD = 2d_{hkl}\sin(\theta)$, where d_{hkl} is the interplanar distance, and θ in the angle between the incident beam and the atomic planes in the crystal. The Miller indexes h, k, and l, are integers used to denote a family of planes. For constructive interference one obtains

$$n\lambda = 2d_{hkl}\sin(\theta), \tag{5}$$

where n is an integer, and λ is the radiation wavelength. The X-ray diffraction – XRD – peaks for a given sample are obtained by focusing an X-ray beam on a crystal, and measuring its intensity as a function of the incident angle θ.

A *Rigaku Smartlab X-ray Diffractometer* was used in this work to obtain the diffraction pattern of magnetostrictive thin films, using a Bragg-Brentano configuration and copper for X-ray production.

3.2.3 Vibrating Sample Magnetometer

Vibrating sample magnetometer – VSM – is a system used to measure magnetic properties of materials, being the materials in bulk, thin film, powder or liquid form. The measurements can be performed as a function of magnetic field, temperature or time. A cooling system is used to control the temperature of the VSM, allowing measurements to be made at a broad temperature range. A schematic of a VSM system is depicted in Figure 3.13.

The sample to be measured is placed on the tip of a long sample holder and fixed with *teflon*. The sample holder is then introduced inside the VSM system, so that the sample is positioned between the pick up coils. A uniform magnetic field H is generated using an electromagnet or a superconducting magnet, inducing a magnetic moment in the sample. The sample is then mechanically vibrated through a vibration system, which could

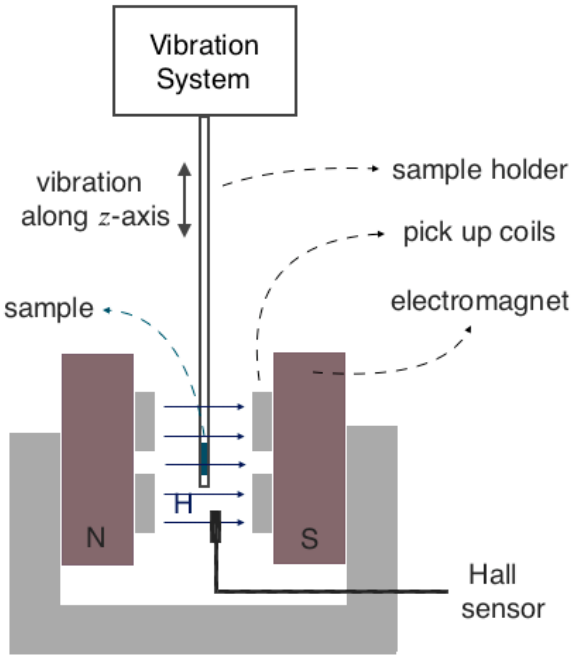

Figure 3.13: Schematic of a VSM system.

be a motor, loudspeaker or piezoelectric transducer. These vibrations cause a magnetic flux variation, which induces a voltage in the sensing coils that is proportional to the magnetic moment of the sample [53]. The induced voltage is measured by a lock-in amplifier connected to a computer. This yields a plot of the magnetic moment of the sample as a function of the parameter of interest, and the magnetization can be measured by dividing the magnetic moment by the mass or volume of the sample. Generally, a Hall sensor inside the system allows an hysteresis loop to be measured, providing information about the sample over a full magnetic field cycle. Saturation magnetization M_S, remanence M_r, and the coercivity H_c, are some of the parameters that can be extracted from the hysteresis curve and that allow for the characterization of the magnetic properties of a sample.

3.2.4 SQUID

The superconducting quantum interference device – SQUID – is an extremely sensitive sensor of magnetic flux. The working principle of this device is based on the tunneling of electrons across a narrow barrier – Josephson junction – between two superconductors. Due to its low threshold ($10^{-18}T$ in some cases), the SQUID is largely used for biological purposes, such as neural activity measurements inside brains.

A superconducting current flows through a ring-shaped flux sensor [Figure 3.14] and,

in the absence of an external magnetic field, the current I_0 divides itself equally between the two paths of the ring and the two Josephson junctions. When an external magnetic field is applied, a current is generated and starts flowing in the ring to generate a magnetic field that compensates the applied external flux. This flowing current in the ring adds to the initial current on one junction, and subtracts to the other. When the current in either junction exceeds a critical value, a resistance generates in the circuit and a voltage generates between A and B. Since only multiples of flux quanta, Φ_0, can diffuse into the ring, the compensating current leads to periodic voltage drops at the SQUID [36].

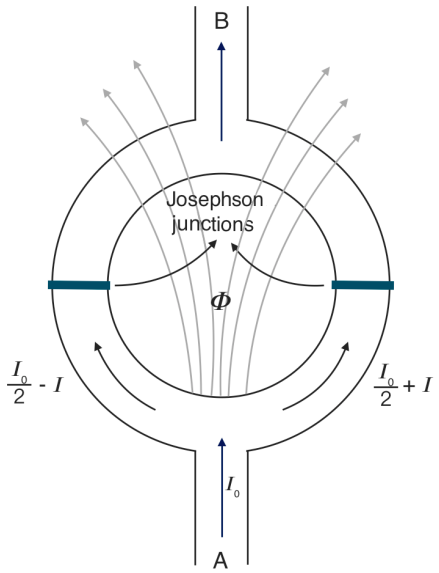

Figure 3.14: Schematic of a SQUID ring used for magnetic flux sensing.

To measure the magnetic moment, a sample is placed and slowly moved inside pick-up coils, and its magnetic moment induces an alternating magnetic flux in the coils. The magnetic flux is transferred to the SQUID ring, which is located in a helium bath located away from the sample. As described above, the SQUID then converts the magnetic flux into a voltage readable by a magnetometer electronics.

The SQUID presents some advantages over other magnetometers due to their highest sensitivity ($10^{-8} emu$ compared do the usual $10^{-4} emu$ for a VSM, for example) and the possibility to operate in a variable temperature range [53].

3.2.5 Profilometer

Profilometry is a technique used to obtain topographical information about a sample. In thin films, it is a valuable method for measuring thickness and surface roughness. Pro-

filometers use a cantilever-shaped tip that moves vertically, to account for surface variations, and laterally, to scan the sample surface in 2D. They are mainly divided into two types – contact and non-contact profilometers. In contact profilometers, the tip is in contact with the sample and its variation in height is measured monitoring the force that the sample exerts on the tip. Since the tip is in close contact with the sample at all times, this technique is slower than other techniques. Also, the tip dimension defines the lateral resolution of the scanned topography. Vertical resolution can achieve sub-nanometer values. For non-contact profilometry, the tip moves vertically without ever touching the sample. One way of determining the position of the tip is by focusing a laser beam on the cantilever surface. Its vertical movement deflects the reflected laser beam, making it possible to register the topography of the sample surface via a photodetector. With this technique, since the tip doesn't touch the surface, the probe tip doesn't wear off, and the scanning velocity is higher and only limited by the speed of the light acquisition detector.

A *Dektak XT* profilometer from *Bruker* was used in this work to measure the thickness of magnetostrictive thin films.

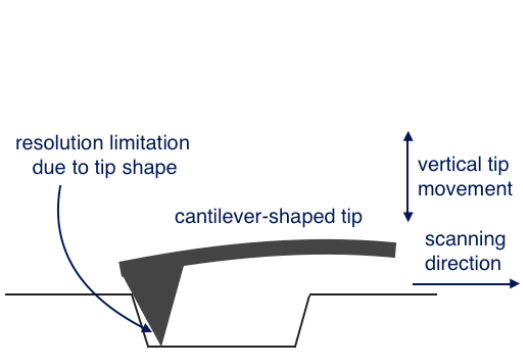

(a) Contact profilometry – resolution limitation due to the shape of the probe tip.

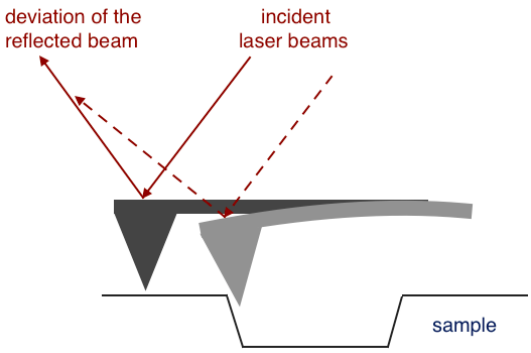

(b) Non-contact profilometry; schematic of a laser system to measure vertical displacement of the cantilever-shaped tip.

Figure 3.15: Schematic of the contact and non-contact methods used in profilometry.

3.3 Taper Fabrication Techniques

Fabrication parameters influence the profile of the taper, which in turn influences the type of application of a specific taper configuration. For example, long linear profile tapers are more suitable for optical tweezers, due to their capability of converging a high intensity evanescent field at the waist region. Birks and Li [1] developed a theoretical model for the shape of tapered optical fibers, in which the modification of a parameter α characterizes a

different profile. α is a constant that relates the length of the heated section and the final taper elongation.

Taper transition radius [1]:

$$r(z) = r_0 \left[1 + \frac{2\alpha z}{(1-\alpha)L_0}\right]^{-\frac{1}{2\alpha}}$$

r_0 – untapered region radius

L_0 – taper waist length

z – tapering direction

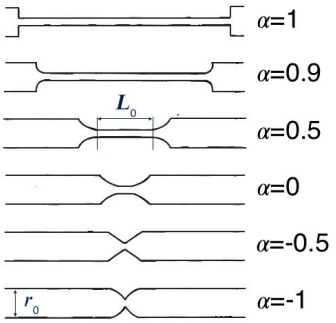

Figure 3.16: Taper shapes for different α; from Birks, *et al [1].*

Over the years, many tapered optical fiber fabrication techniques have been developed, both theoretically and experimentally. Among others, flame or gas burner [8, 54], electric-arc [55], chemical etching [56], and CO_2 laser ablation [57] are reliable techniques for the fabrication of tapers with micrometric waist diameters.

For this project, four techniques were used to fabricate taper tips. CO_2 laser ablation, Vyctran, Ring of Fire, and focused ion beam (FIB) milling are described in detail bellow. While the first three allow the fabrication of tapered optical fibers, the latter is used to create and polish flat top tapered optical fibers tips. Unlike other methods, these methods do not contaminate the optical fiber with by-products of combustion or leave any non-uniformities in the waist region [58].

3.3.1 Laser Ablation

CO_2 laser ablation is a technique that allows the fabrication of low-loss and clean tapered optical fibers with resolution up to $50\,nm$ [57, 58]. For the fabrication of a taper, an uncoated optical fiber is kept at constant tension, fixed between two translation stages that are free to move towards or against each other. A high-frequency CO_2 laser is used as a heat source, and its infrared emission, around $10.6\,\mu m$, is absorbed by silica, melting the fiber in the region where the beam is focused. This focusing on the optical fiber, with the desired spot size, is achieved using a lens and a mirror. To fabricate the taper, both the translation stages and the CO_2 laser must be operated simultaneously. The two translation stages move linearly, pulling the heated fiber, thus achieving good uniformity in the heat

region [58].

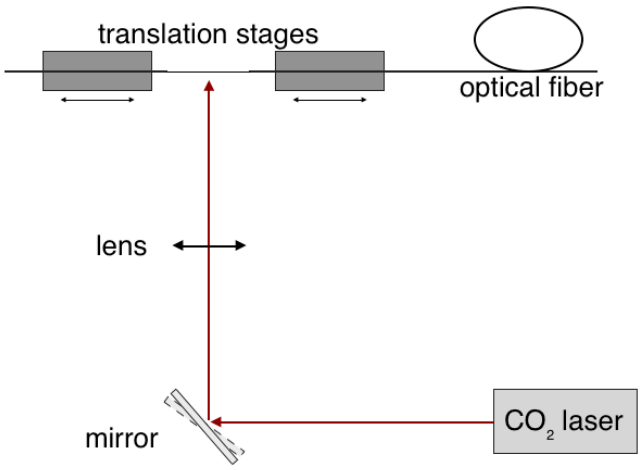

Figure 3.17: Schematic of the CO_2 laser configuration for tapered optical fiber production.

The power of the laser, duration of exposure, and velocity of both translation stages, all contribute to the taper size and shape [59]. Usually, these parameters are controlled by a computer running LabVIEW or a similar software.

3.3.2 Vyctran

Vyctran Processing System is a glass processing platform used to fabricate high-quality fusion splicing and tapered optical fibers. It is mainly comprised of a filament tower, two fiber holding blocks, a microscopic high resolution CCD imaging system, and a computer with an integrated software to control the system [Figure 3.18a].

The fiber holding blocks are two structures that move along the same orientation, and also in the same direction, therefore allowing for the fabrication of single-directional tapers only. While one of the holding blocks moves at a constant speed – pull holding block, the other one moves at a varying speed in order to achieve the desirable taper configuration – feed holding block. Each fiber holding block has a constituent fiber holder with a V-shaped groove where the fiber lays. The fiber is fixed in the fiber holder with both a soft suction produced by a vacuum pump, and a small magnetic clamp.

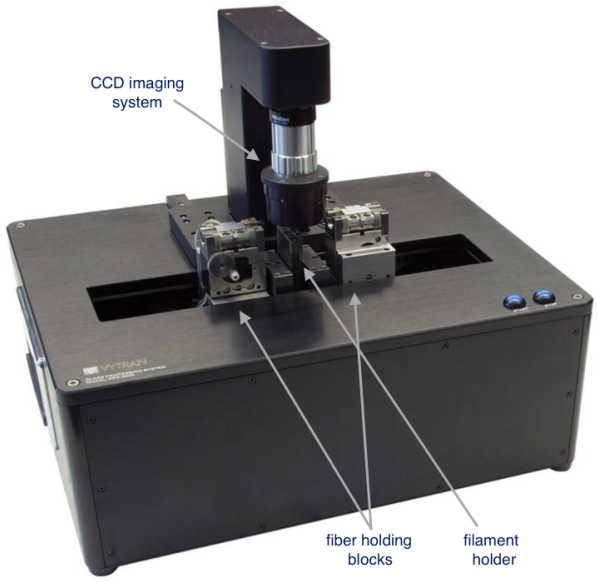

(a) Vyctran Processing System – taken from the user manual.

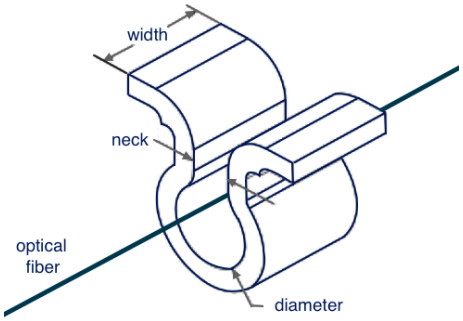

(b) Omega-shaped filament – adapted from the manual.

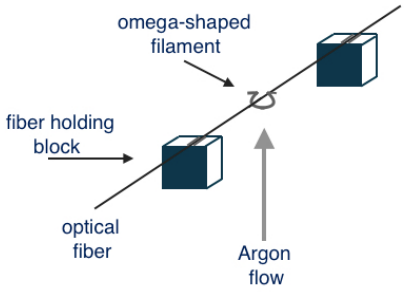

(c) Schematic of the Vyctran system with an optical fiber included.

Figure 3.18: Vyctran Glass Processing System.

The filament tower is comprised of an omega-shaped resistive heater [Figure 3.18b], and is placed between both fiber holding blocks. Several materials can be used as a filament, but in this case a graphite filament was used. Graphite has a melting temperature around $4300K$, higher than the one of tungsten, but evaporates less material during the heating process, leaving less impurities in the fiber. The diameter of the filament is chosen depending on the fiber which is being tapered, being that a filament with a diameter of $2.4mm$ was used for fibers with a $125\mu m$ diameter. The filaments have a $3mm$ width, which limits the minimum waist length that can be obtained.

A taper is created when an optical fiber is fixed in both holding blocks and passing through the center of the filament [Figure 3.18c]. When the fiber is heated until its softening point under a tensile stress, the fiber elongates and its diameter is reduced accordingly.

The filament tower can also move back and forward between the two fiber holding blocks, so that the fiber is heated multiple times until the desired taper diameter is reached. A traveling heating source produces lossless and symmetric tapers, with a constant waist diameter [54]. Below the filament, an Argon flow is applied upwards in order to clean the filament tower and to prevent the oxidation of the filament [Figure 3.18c].

The system is controlled using a software that allows for the adjustment of many parameters. Concerning the taper shape, parameters such as diameter, and up, down and waist region lengths can be tuned. Other parameters can be controlled, for example the pull velocity – velocity of both holding blocks, initial power supply, delta – percentage reduction on the power supply during taper waist fabrication, and hot-push delay – time gap between the beginning of the filament heating and the beginning of the holding blocks movement. The system also incorporates a CCD imaging system that allows the tapering process to be followed in real time.

The disadvantage presented by this system is the need for calculating the start position of both holding blocks and the filament holder before introducing the optical fiber, and introducing these values manually in the software. Also, since the filament has a $3mm$ width, the taper waist must have at least $3mm$ in length, making it impossible to use this system to fabricate tapers without a waist region.

In this work a *JPX-3200* Vyctran was used to fabricate symmetrical tapers with diameters ranging from $10\mu m$ to $18\mu m$, and lengths between $20\mu m$ and $35\mu m$. However, this machine allows for a much wider range of both diameter and taper length.

3.3.3 Ring of Fire Technology

The Large Diameter Splicer – LDS – system is a highly sophisticated fiber processing station by 3SAE Technologies, Inc. This system incorporates the Ring of Fire technology and positioning features. Real-time fiber position and shape can be monitored with two cameras that are placed on top and behind the fiber.

3SAE Ring of Fire technology is a three electrode system organized in a triangular two-dimensional design. The Ring of Fire is aligned with two translation stages and placed between them, so that an optical fiber can be clamped in both translation stages and pass through the center of the three electrodes. This electrode triangular system provides a highly controllable plasma discharge that surrounds the fiber around its circumference, allowing for an even heat distribution.

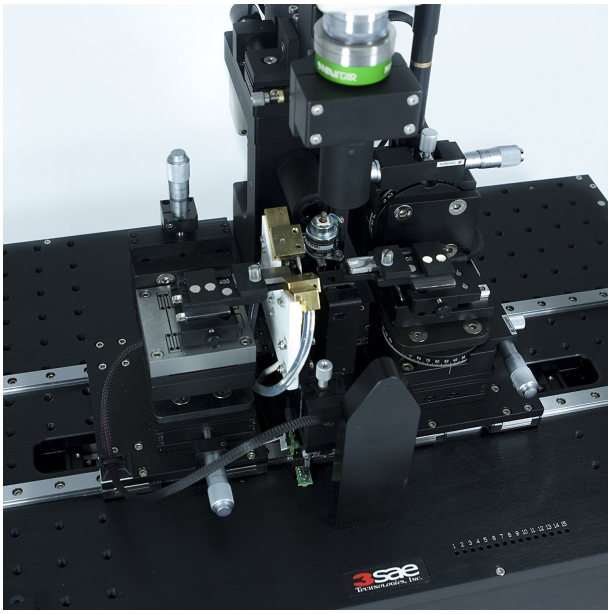

(a) Large Diameter Splicer 2.5 system – taken from the User Manual.

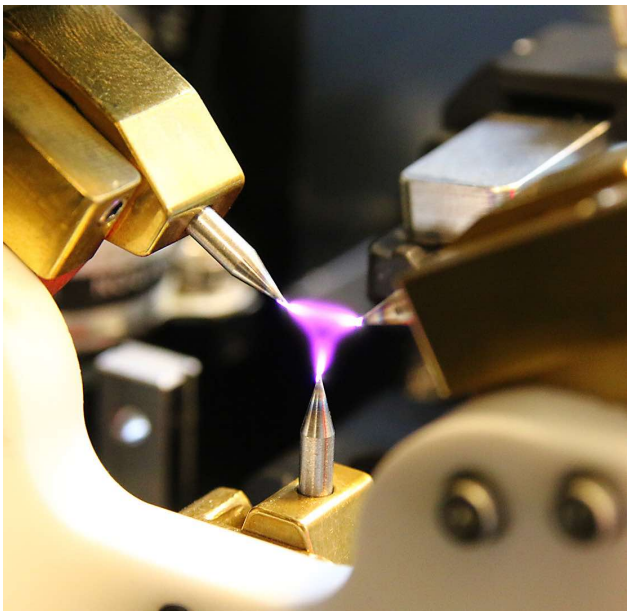

(b) Ring of Fire plasma field.

Figure 3.19: Large Diameter Splicer system by 3SAE.

With the Ring of Fire, splicing – fusing of two fibers, cleaving – fiber cutting, tapering – lowering of the diameter of a fiber, fiber bundling – assembling fibers together side by side into a cable, and fiber diameter scanning can be performed. For splicing, fibers with diameters ranging from $125\mu m$ to $2.5mm$ can be fused together. Even two fibers with different diameters or different shapes can be spliced with high accuracy and low loss. The alignment of the fibers is achieved through the top and side cameras.

For this work, the Ring of Fire was used to taper $125\mu m$ diameter optical fibers.

The smallest diameter achieved in the taper waist was approximately $2\mu m$. The tapering features enables the fabrication of highly accurate tapers in a variety of geometries. Single direction tapering is achieved moving both translation stages in the same direction, and allows for the fabrication of symmetric and asymmetric linear tapers. For bidirectional taper fabrication, the translation stages pull the fiber in opposite directions while the Ring of Fire sweeps back and forward to create the taper region. This method creates tapers with many different shapes. Figure 3.20 shows the Taper Setup tab in the software of the system, where some parameters can be manually changed to achieve the desired taper configuration. Many more variables can be introduced in other tabs of the software, such as scan distance and length, base speed of the translation stages, and taper arc power.

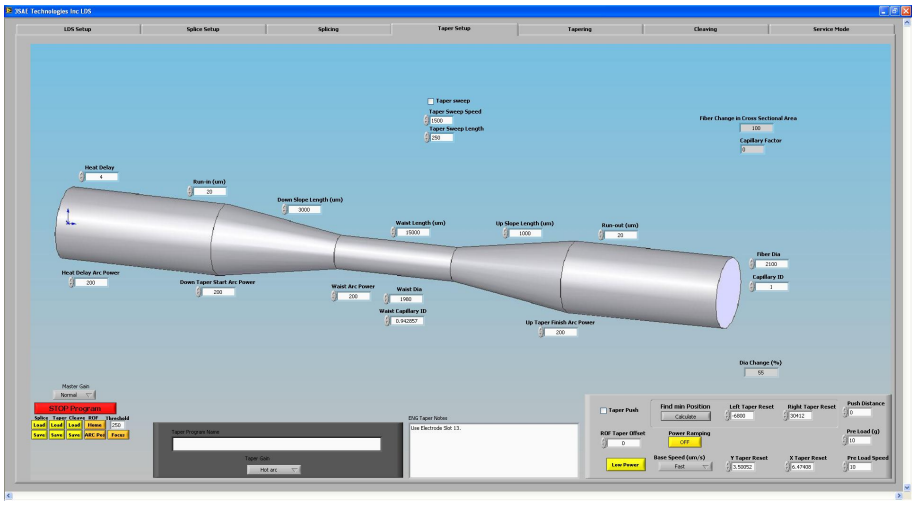

Figure 3.20: Taper Setup tab in LDS software – taken from the User Manual.

With the fiber scan feature, is it possible to obtain the taper profile by moving the fiber in the translation stages and using both top and side camera views. The profile is plotted in a graph like the one in Figure 3.21, representing the diameter of the taper as a function of its length. The scanning can be performed before, after, and during the tapering process, which allows the monitoring of the tapering in real time.

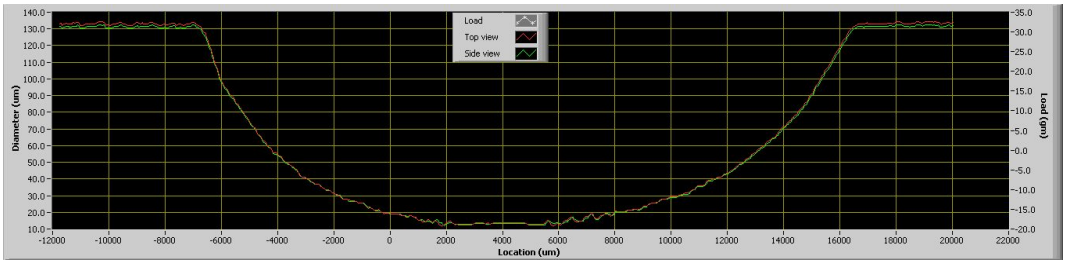

(a) Profile of a symmetric taper with a parabolic profile. This taper was fabricated using the Ring of Fire technology.

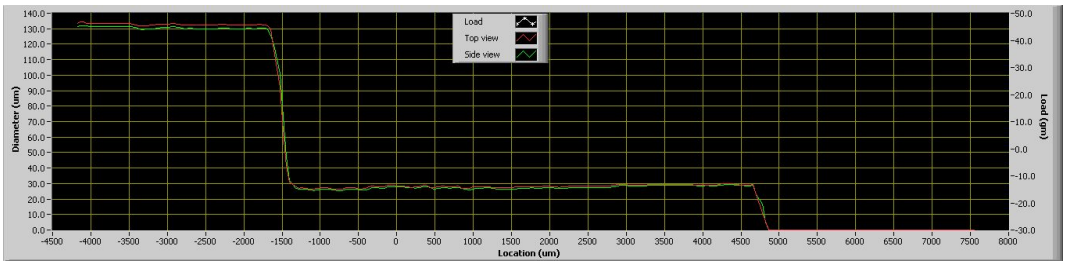

(b) Profile of an abrupt taper tip fabricated with a CO_2 laser.

Figure 3.21: Taper profiles obtained with the scan feature of a LDS system.

3.3.4 FIB Milling

After the fabrication of a taper, two taper tips can be created by cutting a taper in its waist region. The diameter of a taper is typically much smaller than that of a conventional fiber, making it impossible to cut a taper with a standard fiber cleaver. For this reason, the taper is usually cut by hand, which can originate rough edges and irregular surfaces, consequently leading to light scattering and optical signal loss. Due to its nanometric spot size, focused ion beam – FIB – milling is an ideal technology for polishing taper tips and for micro and nano-fabrication [60]. However, this technology can be very slow when the material to mill has higher dimensions, for example a conventional optical fiber with a $125\mu m$ diameter.

FIB milling consists in the ejection of atoms of a substrate, by accelerating ions in the direction of its surface. The accelerated ions are typically metallic ions, specifically gallium ions (Ga^+) accelerated with an energy of about $30\,keV$ [61]. To prevent the accumulation of Ga^+ in non-conducting substrates, such as silica fibers, the substrate is sputter-coated with a thin layer of an electric conductor, such as tantalum or aluminum [62, 60]. After the milling process, the electric conducting layer should be removed by milling the surface with a low current ion beam, or by submerging the exposed taper in an acidic solution.

In this work, a FIB-SEM (focused ion beam - scanning electron microscope) *Lyra*3

XMU system by *Tescan* was used to create a big variety of taper based sensors. This system is comprised of a chamber, inside of which the sample is placed. The dual system has a SEM column - electron beam – for high resolution imaging, and a FIB column – ion beam – for the milling process. The focal point of both electron and ion beams are nearly coincident, enabling SEM imaging and FIB milling to operate simultaneously. The taper tips were fabricated focusing the ion beam on the taper, using a milling pattern. During the milling process, the ion beam sputters atoms from the taper, inside the 2D milling pattern and in depth. This technique allows for a well-defined and high precision circular geometry on the surface of the taper tip [59]. The following figures depict a taper tip fabricated with CO_2 laser and FIB milling.

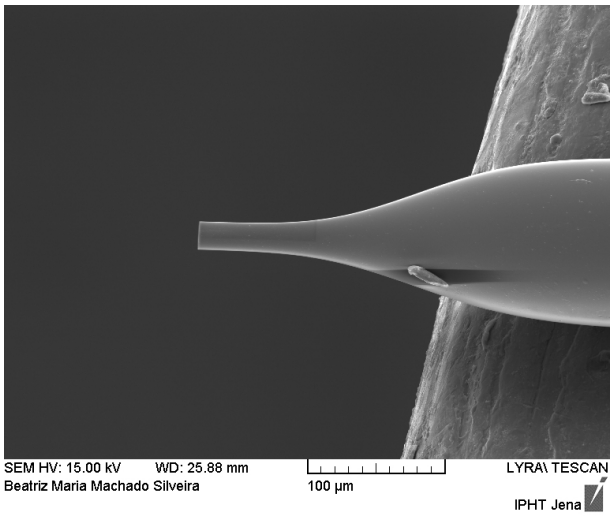

(a) Taper tip – SEM imaging.

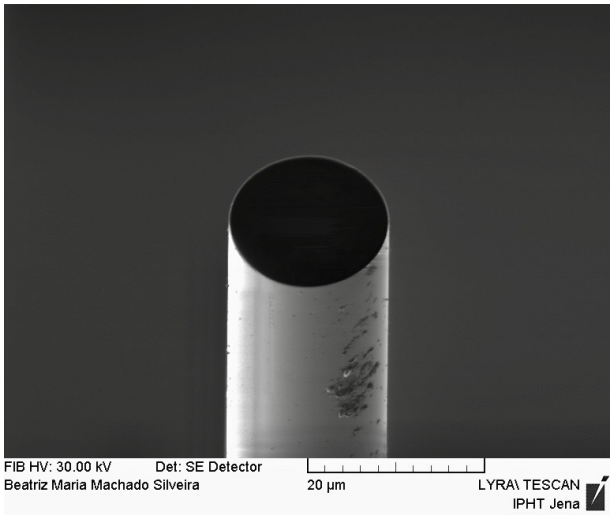

(b) Taper tip – FIB imaging.

Figure 3.22: Taper tip polished using FIB milling.

3.4 Optical Characterization of Microcantilevers

In Section 2.1.2 – *Detection Methods*, many techniques for the detection of mass and resonance frequency shifts in microcantilevers were briefly discussed. All of them are based on the deflection of a microcantilever, in response to an external applied stimulus. This stimulus can be the presence of a specific biomolecule or other particles in liquid or gas, or a change in temperature, pressure, humidity, radiation, etc.

Optical detection methods are divided into two types: contact and non-contact methods. The former includes the *tuning fork resonator* method [63] and the *extrinsic fiber-optic Fabry-Perot Interferometer* [2], and the latter is comprised of a *laser Doppler vibrometer* and an *optical displacement meter* [64].

Particularly in this report, two non-contact, high-resolution optical systems will be used for the characterization of microcantilevers with a deposition of magnetostrictive $Co_{66}Fe_{34}$ thin films: a system comprised of a laser and a 4-quadrant photodetector, and a Fabry-Perot interferometer. These methods allow for non-evasive remote monitoring of the characterization systems. The characterization of the microcantilevers consists in the measurement of deflection of their free end when an external magnetic field is applied.

3.4.1 Position Sensitive Photodetector

A 4–quadrant photodetector is a type of position sensitive detector, PSD, comprised of four active photodiode sensors. They are used to detect and measure extremely small position displacements of an incident light beam. These detectors present a nanometric resolution which, similarly to their sensitivity, decreases with increasing optical path [65] and with increasing spot size [66].

Microcantilever characterization systems using photodetectors, generally use a collimated laser source to shine light on the surface of the microcantilever near its tip When the reflected light is incident on the photodetector, a photocurrent is detected by each sensor. Applying an external magnetic field, the magnetostrictive material causes a deflection on the tip of the cantilever, deviating the reflected beam from its former direction. The distribution profile on the photodetector changes in both x and y directions, allowing for the measurement of the displacement of the microcantilever [37].

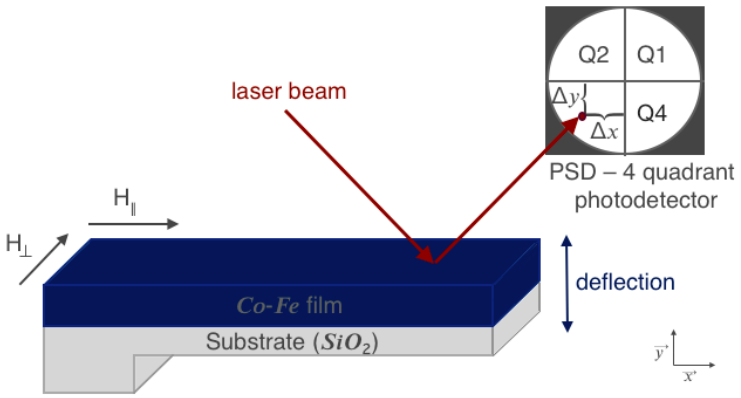

Figure 3.23: Schematic of a magnetostrictive microcantilever characterization system using a 4-quadrant photodetector.

The normalized displacement coordinates, (X, Y), for the location of the laser beam on the photodetector are given by:

$$\begin{cases} X = \frac{(Q2+Q3)-(Q1+Q4)}{Q1+Q2+Q3+Q4} \\ \\ Y = \frac{(Q1+Q2)-(Q3+Q4)}{Q1+Q2+Q3+Q4} \end{cases}, \tag{6}$$

where $Q1$, $Q2$, $Q3$, and $Q4$, are the photocurrents detected by each sensor.

3.4.2 Fabry-Perot Interferometer

Fabry-Perot – FP – interferometry is based on the interference of multiple light beams in an optical cavity. In the simplest case, the optical cavity is formed by two partially reflecting surfaces, parallel to each other. In the particular case of this work, in order to measure deflection in magnetostrictive devices, a tapered optical fiber tip can be used to shine light orthogonally onto the surface of a magnetostrictive microcantilever. The light beam is partially reflected in the cleaved tapered tip, and again partially reflected in the magnetostrictive surface of the microcantilever [Figure 3.24].

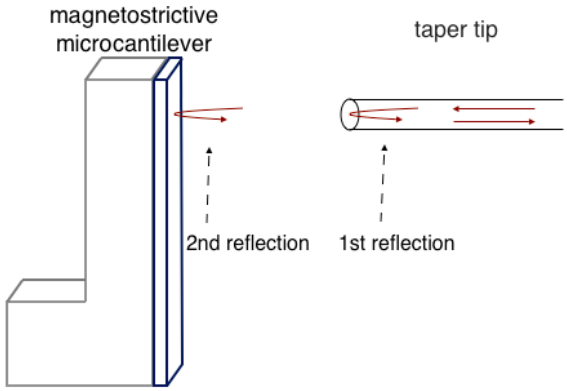

Figure 3.24: Schematic of a Fabry-Perot interferometer, using a magnetostrictive microcantilever as a reflecting surface, and a taper as a light source.

Since both surfaces act as reflecting surfaces, the system behaves as an FP interferometer [67]. The resulting reflected signal is the interference of both reflected beams, which is then guided back through the optical fiber, and analyzed in a spectral measurement device, such as an optical spectrum analyzer, OSA. When the two reflected beams are in phase, constructive interference occurs and a maximum peak appears in the reflection spectrum. Likewise, when the two signals are out of phase, destructive interference takes place and a minimum peak shows in the spectrum. Therefore, the typical spectrum of a FP cavity is a fringe-like spectrum with alternating maximum and minimum peaks. The phase difference between the two reflected signals, φ, and the cavity length, L, are given by the following equations:

$$\begin{cases} \varphi = \frac{2\pi}{\lambda} 2nL \qquad (a) \\ \\ L = \frac{\lambda_1 \lambda_2}{2nFSR} \qquad (b) \end{cases} \tag{7}$$

where λ is the operational wavelength, n is the refractive index of the cavity medium, λ_1 and λ_2 are the wavelengths of two consecutive fringe minima, and $FSR \equiv \Delta\lambda = \lambda_2 - \lambda_1$ is the free spectral range.

When a magnetic field is applied to the system, the magnetostrictive thin film causes a deflection on the microcantilever, changing the value of L. It is then possible to measure the change in the cavity length, ΔL, as a function of the applied magnetic field, which corresponds to the deflection of the microcantilever.

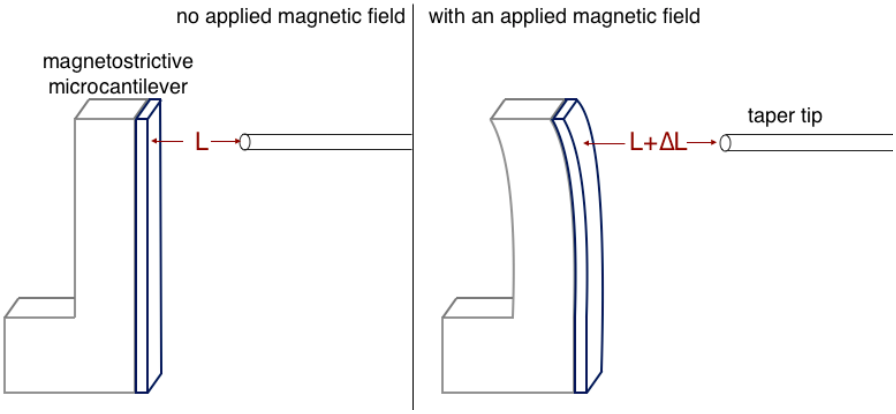

Figure 3.25: Schematic of a magnetically actuated magnetostrictive microcantilever, and the consequent change in the cavity length, L.

Fabry-Perot interferometers present high sensitivity, reduced size and cost, immunity to electromagnetic radiation, and can be used in critical environments [67].

Chapter IV

Fabrication and Characterization of a Magnetostrictive Microcantilever

In this chapter, the microfabrication of magnetostrictive films and magnetostrictive microcantilevers is described in detail. Following the fabrication process, the samples are investigated in terms of their structural and magnetic properties. Finally, an optical system to measure microcantilever displacement is reported. The characterization method uses a laser and a PSD to measure deflection in the microcantilevers, and is based on the optical path change of a light beam upon reflection on the tip of a microcantilever.

4.1 Magnetostrictive Thin Film Deposition by e-beam Evaporation

Prior to the fabrication of a die of magnetostrictive microcantilevers, magnetostrictive thin films were prepared and characterized. An *Edwards Auto* 306 evaporator was used to deposit a $Co_{66}Fe_{34}$ thin film on a hydrogenated amorphous silicon layer, $n^+a-Si:H$, the same material which made up the microcantilever structure. The stoichiometry for the $Co-Fe$ alloy, $Co_{66}Fe_{34}$, was chosen for its highest magnetostrictive effect [37]. A sketch of the evaporator chamber is found in Figure 3.9 (Subsection 3.2.1 – *Electron Beam Physical Vapor Deposition*).

A *Corning Glass* substrate with a deposited hydrogenated amorphous silicon layer, $n^+a-Si:H$, was placed underneath the deposition plate, and fixed using *kapton*. The target material was a $99,999\%$ pure $Co_{66}Fe_{34}$ sample produced by arc melting. The target was placed in a copper crucible and the target plate was rotated so that the target was placed beneath the tungsten filament. Initially, the chamber was at room temperature. A rotary pump was used for rough pumping, until about $3 \times 10^{-5} mbar$, and to back the turbomolecular pump, responsible for achieving high vacuum, of approximately $7 \times$

$10^{-6}mbar$. A $10mA$ current and a $4kV$ voltage were applied to the filament. When the crucible was incandescent, the shutter was open to allow the vapor cloud to reach the substrate. To prevent the magnetostrictive thin film to reach high temperatures during the evaporation process, its deposition on the hydrogenated amorphous silicon was carried out in small time intervals of 3 minutes, in a total of 72 minutes, with 5 minute intervals between each deposition. This methodology was chosen based on previous and already optimized tests performed at IFIMUP. The total amount of 72 minutes was chosen to achieve the desired thickness. Using a *Dektak XT* profilometer from *Bruker*, a thin film thickness of approximately $136nm$ was measured.

For simplicity, this sample, comprised of a $Co_{66}Fe_{34}$ layer deposited on $n^{+}a-Si:H$ at room temperature, will be denoted as $SiMag-r$.

4.1.1 Atomic Structural Characterization of a Magnetostrictive Thin Film

XRD was performed on the magnetostrictive thin film to investigate the presence of a crystalline phase. Figure 4.26 depicts an XRD pattern for the $SiMag-r$ sample, obtained with a *Rigaku Smartlab X-ray Diffractometer*. Copper was used as a material for X-ray production, yielding a wavelength radiation of $\lambda(CuK_{\alpha}) = 1.5418$Å. A Bragg-Brentano geometry was used. The intensity of the diffracted X-rays is plotted as a function of the diffraction angle (2θ).

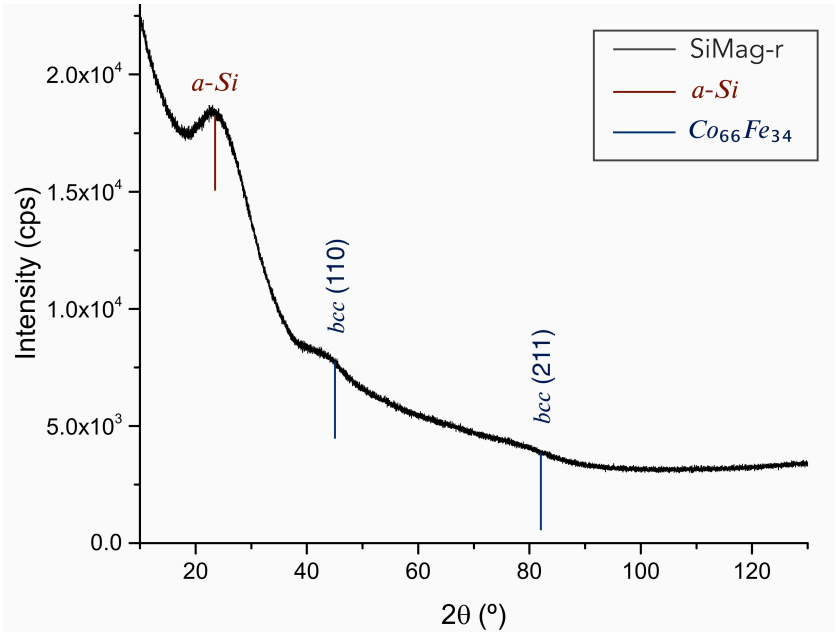

Figure 4.26: X-ray diffraction patterns for the sample $SiMag-r$ – hydrogenated amorphous silicon with a $Co_{66}Fe_{34}$ deposition, deposited at room temperature.

By comparison with literature, it was possible to discern the diffraction peaks marked in the plot. The hydrogenated amorphous silicon layer can be seen as the broad distribution around $2\theta \approx 23^\circ$. Another two broad peaks are present, which coincide with the $bcc\,(110)$ and $bcc\,(211)$ phases of the magnetostrictive $Co_{66}Fe_{34}$ film, yielding a polycrystalline $Co_{66}Fe_{34}$. The fact that two broad bands are present, instead of two narrow diffraction lines, is associated with the small grain size, or even an underdevelopment of the grains, *i.e.*, recrystallization was not complete and grain growth was limited as a result of a thin film deposition at lower temperatures (room temperature, in this case).

4.1.2 Magnetic Characterization of a Magnetostrictive Thin Film

A *MPMS EverCool* SQUID by *Quantum Design* was used to obtain the hysteresis curves for the $SiMag - r$ sample at room temperature. The sample was wrapped in cotton, to prevent it from moving, and enclosed in a small capsule. The capsule was introduced inside a long sample holder which was then vertically placed inside the SQUID system. To ensure that the sample was located exactly between the coils, a $1000Oe$ field was applied and the sample was slowly moved downwards in the system. Using a computer with the system's software, the magnetic moment, m, as a function of the distance was plotted. The positioning of the sample in the center of the coils should coincide with the highest magnetic moment obtained through the full DC scan. The following plot shows the magnetization of the sample, or magnetic moment per unit volume, as a function of the applied magnetic field, at $300K$.

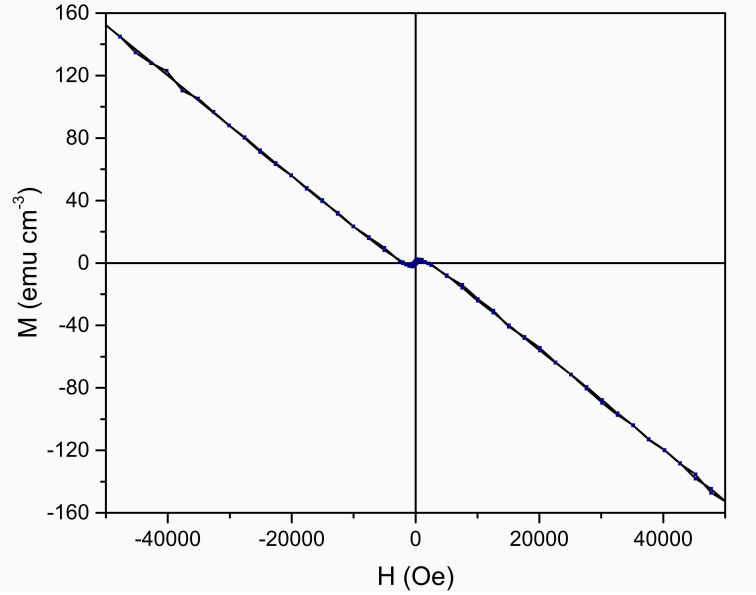

Figure 4.27: SQUID measurement of magnetization as a function of magnetic field, for the sample $SiMag - r$ – deposition of a magnetostrictive thin film on amorphous silicon, at room temperature.

The plot depicts a linear relation between the magnetization and the magnetic field, and the steep slope is attributed to the diamagnetic properties of the substrate. By extracting the linear contribution from the diamagnetism, the magnetization of the thin film is obtained.

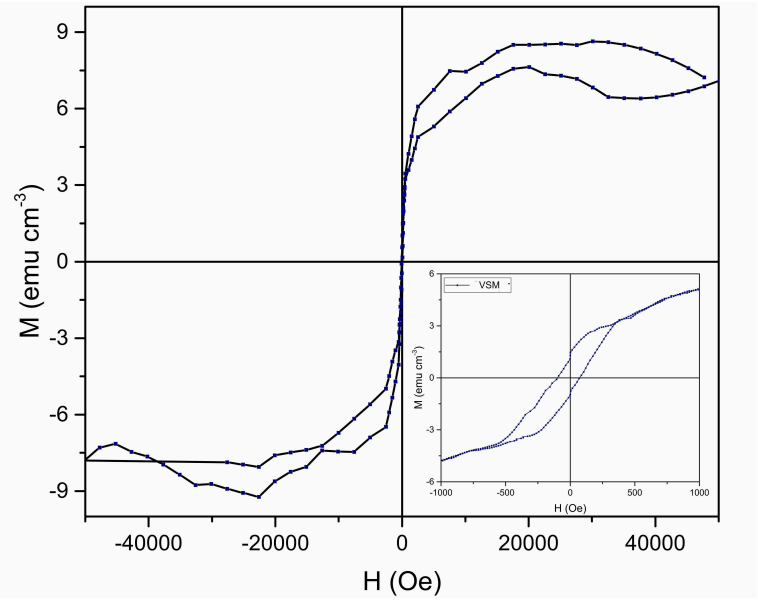

Figure 4.28: SQUID measurement of magnetization as a function of magnetic field, for the sample $SiMag - r$. The inset plot shows a VSM measurement with a more detailed view around the coercive field.

Through the plot, the ferromagnetic nature of the sample can be perceived, despite the noisy signal. However, the lack of resolution near the center doesn't allow the confirmation of a hysteretic behavior. For this reason, a detailed VSM measurement was performed around the center to confirm the hysteresis. The sample was fixed in a sample holder using *teflon*, and introduced inside the system. The centering of the sample was done at a $1000Oe$ field. After centering, the hysteresis curve was plotted for $|B| \leq 10\,000Oe$. The magnetic field was changed by no more than $3000Oe/min$. The result is depicted as an inset plot in Figure 4.28. A hysteresis is in fact present, thus confirming the ferromagnetic character of the thin film. As seen from the plot, the coercive field, H_c, was approximately $100Oe$. Hunter *et al.* measured the coercivity for a $5\mu m$-thick $Co_{66}Fe_{34}$ film, deposited in a Si/SiO_2 substrate at room temperature, and obtained the value $H_c \approx 110Oe$ [37].

Regarding the saturation, the mean value obtained for the magnetization was $M_S = (8 \pm 1)emu\,cm^{-3}$. The saturation magnetization, M_S, value for bulk $Co_{66}Fe_{34}$ was not found in literature. Nonetheless, the values of bulk Co and bulk Fe were found to be $1424emu\,cm^{-3}$ and $1711emu\,cm^{-3}$, respectively [68]. Comparing these values of M_S with the saturation magnetization value obtained for the deposited $Co_{66}Fe_{34}$ thin film, one concludes that there is at least a $99wt\%$ of amorphous film in the $SiMag-r$ sample, and only about $0,5wt\%$ of crystalline formation is present. This fact corroborates the results obtained by the X-ray diffraction pattern [Figure 4.26].

Despite not holding a high magnetization, the sample exhibits a ferromagnetic behavior and a trend for a magnetostrictive $Co_{66}Fe_{34}$ thin film can be expected. For this reason, it is reasonable to predict the bending of the microcantilevers if a $Co_{66}Fe_{34}$ film was deposited on its surface.

4.2 Microcantilever Microfabrication

The $SiMag-r$ sample, previously characterized, showed a tendency for a magnetostrictive behavior. Consequently, a $Co_{66}Fe_{34}$ thin film was deposited on a die of microcantilevers under the same conditions. The fabrication of the magnetic sensitive microcantilevers is herein described.

The microcantilevers were fabricated in a class 10 clean room in *INESC-MN*, Lisboa, Portugal, in collaboration with a colleague, Rui Pinto. To allow for a future analysis of the deflection of cantilevers depending on their dimensions, 162 different dimension microcantilevers were deposited, in a total of 810 microcantilevers. They were arranged

in a die with varying length and width, from $10\mu m$ to $250\mu m$, and from $10\mu m$ to $180\mu m$, respectively.

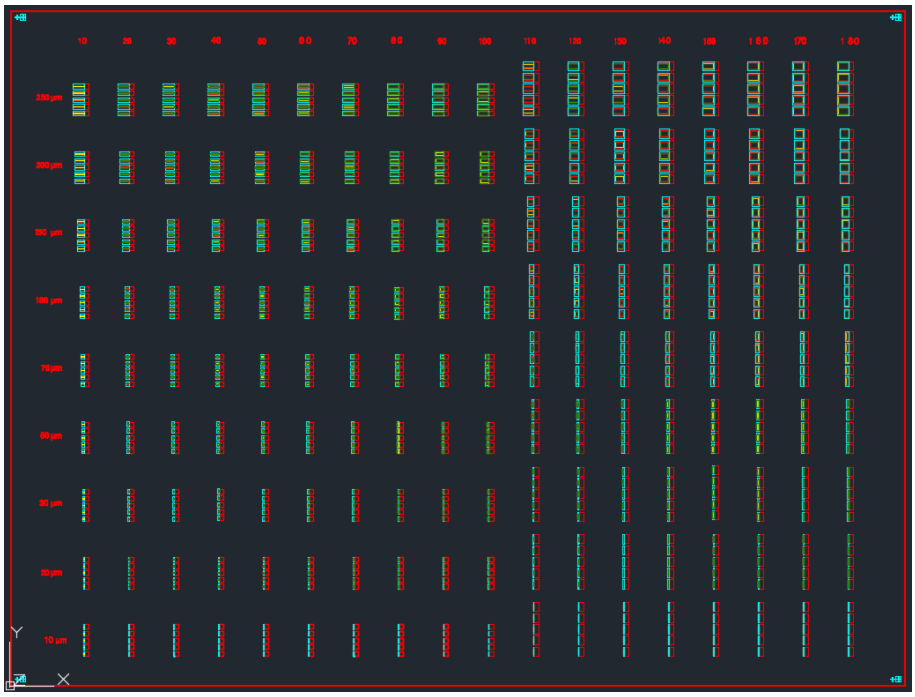

Figure 4.29: AutoCAD scheme of the arrangement of the microcantilevers on the die (dimensions in microns).

The substrate used was a $0.7mm$ thick *Corning Glass 1737*. Its cleaning process started off with rinsing and rubbing the substrate with acetone to remove organic impurities, followed by isopropanol (IPA), to dissolve acetone remains. The substrate was then placed in an ultrasonic bath of *Alconox* detergent for 30 minutes, and again in another ultrasonic bath of deionized water, or DI water. To finish the cleaning process, the substrate was again rinsed with IPA, DI water, and blown dry with compressed air.

Using a *Nordiko 7000* Magnetron Sputtering System, an approximately $1.02\mu m$ thick *Al* sacrificial layer was sputtered on the substrate. A HDMS coating was applied on the sacrificial layer to enhance photoresist adhesion, followed by a positive photoresist spin coating. Using a direct laser writing system, a mask was used to inscribe a pattern on the photoresist, and an appropriate photoresist developer was used to remove the desired photoresist from the film. Finally, a wet etchant was used to remove the exposed aluminum, and the remaining photoresist was removed in an acetone bath. The described procedure was then similarly repeated for the deposition of a hydrogenated amorphous silicon layer, $n^+a-Si:H$, and a magnetostrictive layer. The $n^+a-Si:H$ layer was approximately

$0.85\mu m$ thick, and was deposited by PECVD. The patterning of the layer was structured through reactive ion etching, RIE.

The magnetostrictive thin film was an approximately $136nm$ thick $Co_{66}Fe_{34}$ layer, deposited by EBPVD as described in the previous section (Section 4.1 – *Magnetostrictive Thin Film Deposition by e-beam Evaporation*). For comparison, all the parameters were kept unchanged, such as current, pressure, working distance, and evaporation time. It is important to note that, throughout the deposition of the $Co_{66}Fe_{34}$ thin film on the die, high temperatures should be avoided to prevent photoresist melting and consequently the destruction of the microcantilevers. Moreover, the high coefficient of thermal expansion of Al, in comparison to those of silica and $Co_{66}Fe_{34}$, can also contribute to the damaging of the microcantilevers. The deposition of the magnetostrictive thin film was performed in CEMUP-MNTEC, Porto.

The release of the microcantilevers was achieved using an Al etchant in order to remove the Al layer and thus creating the microcantilever structure. The film was again cleaned using DI water, acetone, IPA, and blown dry using compressed air. Again, for simplicity, the deposition of the magnetostrictive $Co_{66}Fe_{34}$ thin film on the die of microcantilevers at room temperature will be denoted as $McMag - r$. A general schematic with the described deposition steps is presented in Figure 4.30a for one microcantilever. A more detailed process description can be found in the Appendices, including the equipment used, time, pressure, temperature and thickness specifications for all steps of the fabrication.

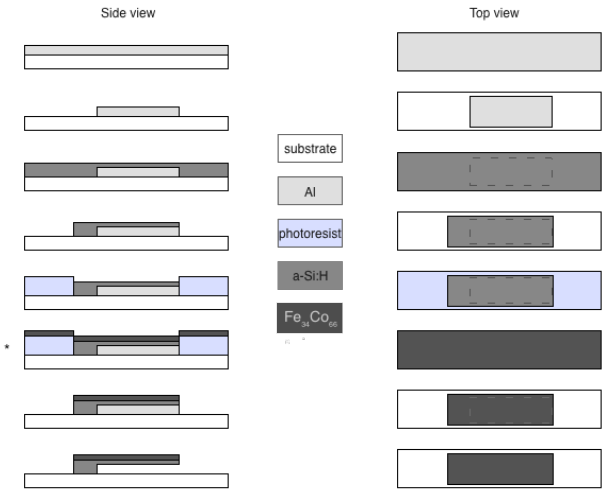

(a) Schematic of some steps of a magnetostrictive microcantilever fabrication process.

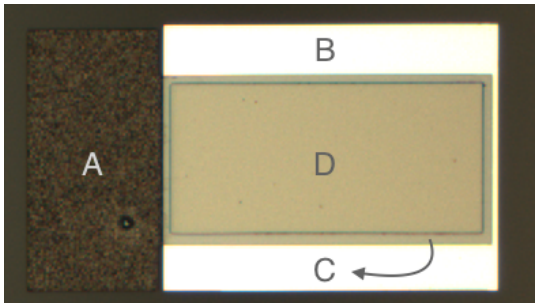

(b) Top view of a magnetostrictive microcantilever.

A – Structural Layer: Corning glass ($0.7mm$ thick)
B – Sacrificial Layer: Al by magnetron sputtering ($1.02\mu m$ thick)
C – Structural Layer: $n^{+}a-Si:H$ by PECVD ($0.85\mu m$ thick)
D – Magnetostrictive Layer: $Co_{66}Fe_{34}$ by e-beam evaporation ($136nm$ thick)

Figure 4.30: Fabrication process of die of microcantilevers and final result.

XRD was then performed on the die of microcantilevers. The aim was not only to characterize the die regarding atomic structure, but also to compare its properties to those of the $SiMag-r$ sample. An optical characterization system was then used to measure deflection of the microcantilevers under an applied magnetic field.

4.2.1 Atomic Structural Characterization of the Microcantilevers

The X-ray diffraction analysis was performed for the die of microcantilevers – $SiMag-r$ sample – before removing the photoresist and the Al sacrificial layer. The diffraction patterns were measured at room temperature and using a Bragg-Brentano geometry. The result is depicted in the diffractogram in Figure 4.31, using copper as the target material for X-ray production, and for a radiation wavelength $\lambda(CuK_{\alpha}) = 1.5418$Å.

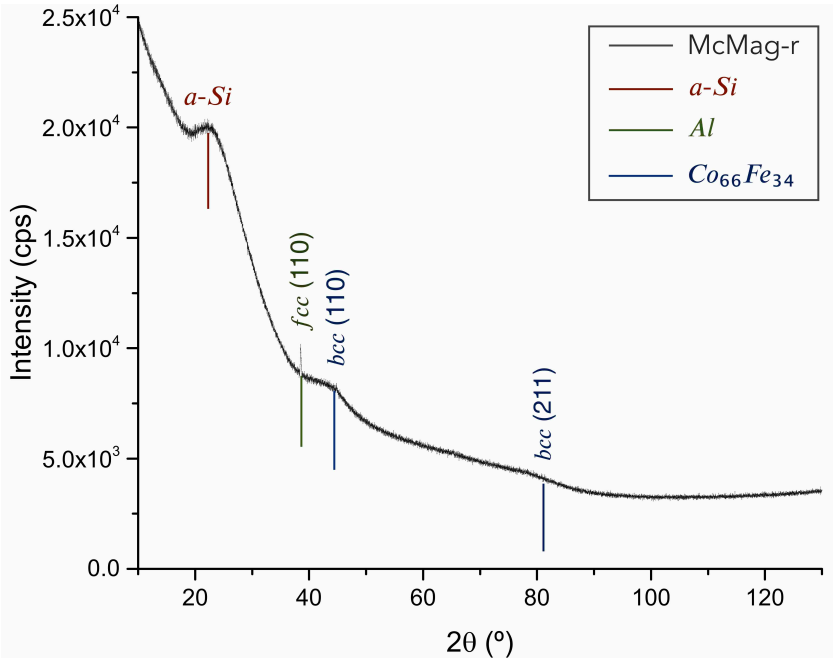

Figure 4.31: X-ray diffraction pattern for the sample $McMag-r$ – die of microcantilevers still with photoresist and an Al sacrificial layer, and a $Co_{66}Fe_{34}$ deposition; deposited at room temperature.

The first broad distribution at $2\theta \approx 23^\circ$ corresponds to the hydrogenated amorphous silicon layer. A narrow Bragg reflection is then present, corresponding to the $fcc\,(110)$ phase of the Al sacrificial layer. The diffraction peaks $bcc\,(110)$ and $bcc\,(211)$ are observed, indicating the presence of a crystalline phase in the $Co-Fe$ film. Comparing this diffraction pattern (for the $Co_{66}Fe_{34}$ film deposited on a die), and the previously shown in Figure 4.26 (for the $Co_{66}Fe_{34}$ film deposited on amorphous silicon), it is possible to deduce that equal deposition conditions promote very similar crystallographic orientations, being that the amorphous silicon and the bcc peaks for the $Co-Fe$ composite are present in both cases. Nonetheless, both peaks are very broad and weak, and their intensity would likely increase if the thin film was deposited at higher temperatures, promoting grain growth.

The magnetic properties of the die of microcantilevers were not analyzed using VSM or SQUID, since the sample was large to fit the sample holder. There was also a risk of removing or damaging the microcantilevers with *teflon* trying to fix the sample. However, since the magnetostrictive film was deposited under the same parameter for both $SiMag-r$ and $McMag-r$ samples, the magnetic properties are expected to be similar in both cases.

4.2.2 Optical Characterization using a Laser and PSD Configuration

To measure the deflection of the microcantilevers by optical means, an optical characterization system was assembled. This setup was based on a characterization system already used by other authors for measuring defection in such structures [4, 31, 37, 69, 70]. This deflection was due to the magnetostriction behavior of the $Co_{66}Fe_{34}$ thin film deposited on the microcantilevers – sample $McMag - r$. Under a magnetic field, the magnetostrictive material has its volume changed, causing the deflection of the microcantilevers. This system incorporates a laser to emit light on the microcantilevers and a position sensitive photodetector to collect the reflected signal.

To measure deflection of the free end of the microcantilevers as a function of the applied magnetic field, the die was placed between two Helmholtz coils, responsible for inducing a magnetic field on the sample. A schematic and a picture of the experimental configuration are depicted in Figure 4.32. The die was placed in a way that the magnetic field was applied parallel to the length of the cantilevers. A *BOP 50-4D* Kepco was used to amplify a sinusoidal signal from an *Agilent 33220A* signal generator, which induced an AC magnetic field in the coils. A collimated laser source ($658nm$, $10\mu W$) was used to shine light on a microcantilever tip, and a PSD (*Eltec 404-4*) was used to collect the reflected signal. The laser beam was pointed at one microcantilever at a time. The magnetic field leads to the change in volume of the magnetostrictive thin film, resulting in the deflection of the microcantilevers. The values R, the amplitude of the measured signal, and Φ, the phase between the signal measured in the photodetector and the reference signal from the signal generator, were obtained by a lock-in (*Stanford Research Systems SR830*), which was connected to the photodetector. Since the AC current in the coils induces a vibrating movement on the microcantilevers, the lock-in was set to be driven at twice the reference frequency to measure the second harmonic. The integration time of the signal ranged from $1s$ to $30s$. A computer with *LabVIEW* was used for data acquisition.

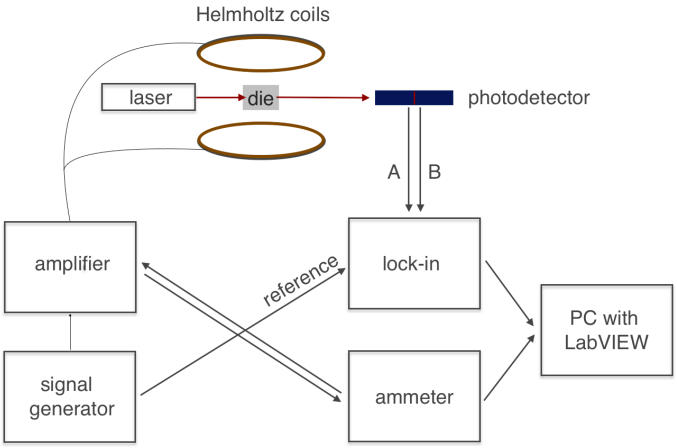

(a) Schematic of the experimental setup.

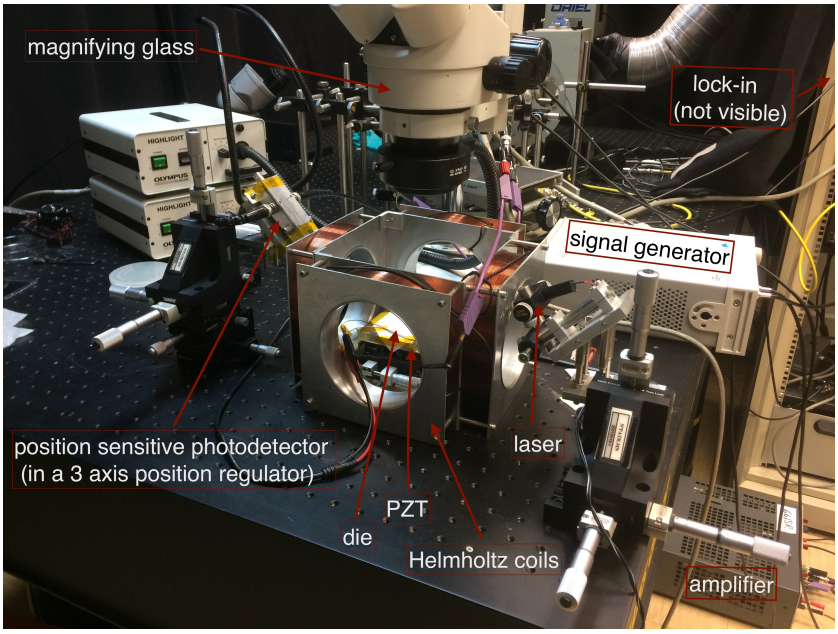

(b) Picture of the experimental setup.

Figure 4.32: Optical experimental setup using a laser and photodetector as the sensing element.

The LabVIEW program returned values of R and Φ as a function of the peak-to-peak amplitude of the generated signal, V_{pp}. To convert the values of R into displacement, a *PSI-5A4E* piezoelectric – PZT – sheet was used to calibrate each microcantilever measured, so this method is in fact an indirect method for measuring deflection. The PZT was placed beneath the die of microcantilevers. The calibration was performed by applying an increasing voltage between the upper and bottom surfaces of the PZT, and measuring the amplitude R of the first harmonic in the lock-in. Due to the compression or tension of the PZT in the direction of the applied tension, the microcantilever being calibrated

accompanies the movement of the PZT, deviating the laser beam from its former position. For this particular PZT, the strain coefficient is $d_{33} = 390 \times 10^{-12} m/V$, for an induced strain in the direction of the applied tension. The values for the applied magnetic field H were obtained through a previously calibration between V_{pp} and H. The calibration was performed by increasing the voltage applied to the Helmholtz coils, and measuring the magnetic field with a Hall probe. The displacement as a function of the applied magnetic field was measured for 6 microcantilevers with different dimensions. However, based on the results obtained, only 3 are herein discussed [Table 4.5].

The following graphs display the displacement and phase signal for each microcantilever as a function of the magnetic field, for different frequencies of the AC input signal in the coils. Figure 4.33 depicts displacement and phase for microcantilever $M1$. The displacement increases almost linearly with the applied magnetic field, until it reaches a saturation point. This behavior is related to the orientation of the magnetic domains of the magnetostrictive material in the direction of the applied magnetic field as it is increased. When all domains are oriented parallel to the field direction, the magnetostrictive material is at its maximum elongation, the displacement is maximum, and saturation is reached.

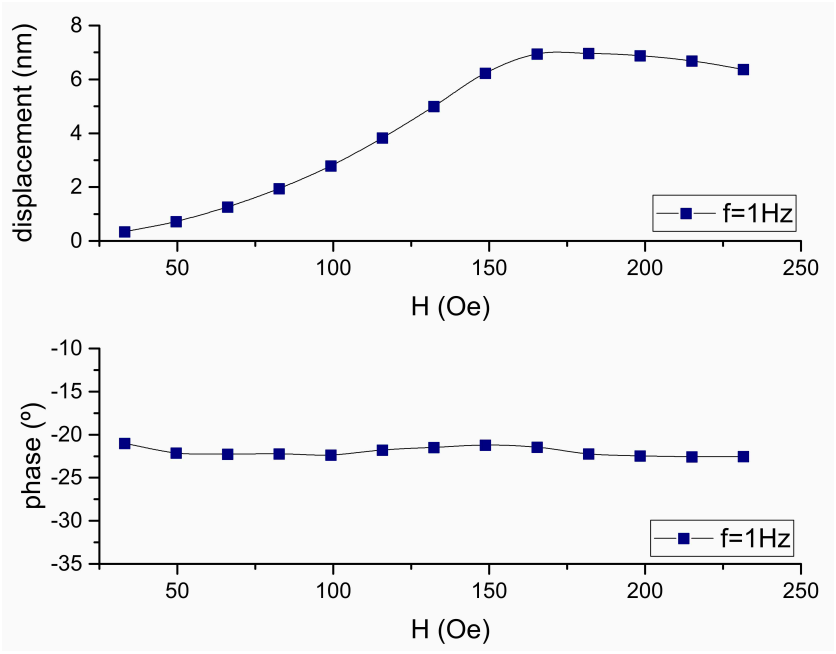

Figure 4.33: Displacement and phase as a function of the applied magnetic field – $M1$.

The effect of frequency was investigated for microcantilever $M2$. For low frequency magnetic fields [Figure 4.34a], the expected behavior for the displacement is obtained, which doesn't occur for higher frequencies [Figure 4.34b]. Comparing both graphs from

Figures 4.34a and 4.34b, one concludes that this steady displacement response corresponds to approximately constant phase signals. The displacement started off by being stable for low frequencies of the applied signal – $1Hz$, $5Hz$, $10Hz$ – and progressively lost stability for higher frequencies – $66Hz$, $113Hz$, $233Hz$ – possibly as a result of inductive, capacitive, and thermal effects introduced in the characterization system for higher frequencies.

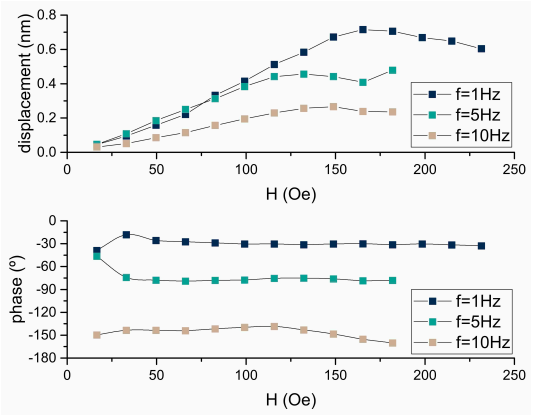

(a) Low frequency signals.

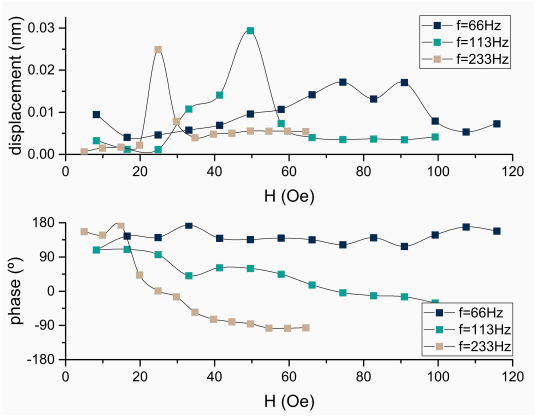

(b) High frequency signals.

Figure 4.34: Displacement and phase as a function of the applied magnetic field, for different frequencies of the AC input signal in the coils – $M2$.

For every microcantilever tested, the magnetic field ranged from $0Oe$ to $250Oe$, which appeared to be sufficient to actuate the microcantilevers until they reached maximum displacement. Previously performed tests, using a different die of microcantilevers, showed that the microcantilevers can easily break and permanently remain damaged when high magnetic fields are applied to the magnetostrictive film. To test the repeatability of the deflection method using this characterization setup, three measurements were carried out using microcantilever $M3$ under the same conditions and for the same frequency. The obtained results are depicted in the figure below. For the first two measurements, the displacement curves almost coincide, despite the field range used being different. For the third measurement, although the curve deviates from the previous ones, the saturation appears for the same value of magnetic field. The reason for this deviation might be related with an increase in the system temperature for the last measurement performed. Despite this divergence, the signals still show high similarities, which evinces that the microcantilevers were not damaged for such low fields and that the microcantilevers return to their initial geometric states after the magnetic field is removed.

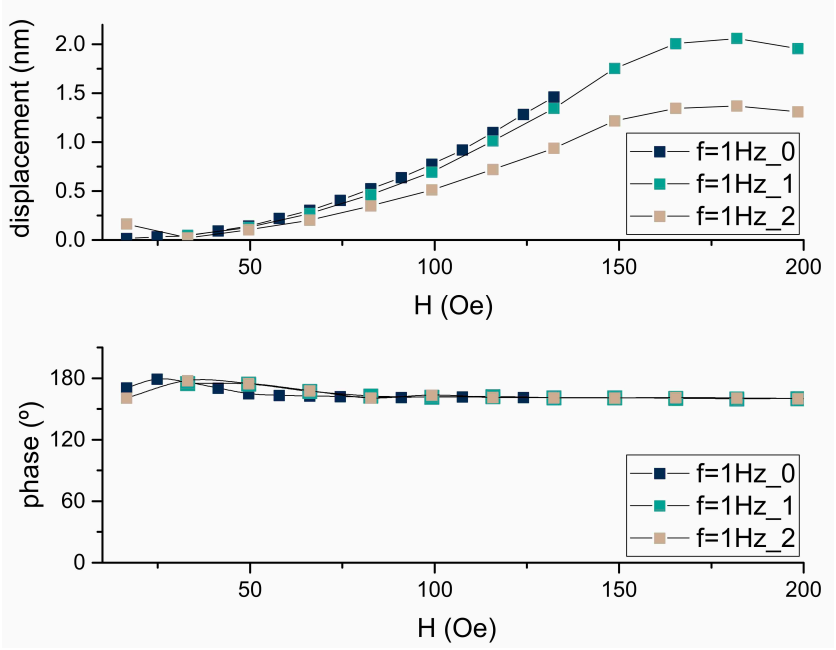

Figure 4.35: Displacement and phase as a function of the applied magnetic field – $M3$.

In Table 4.5, the values of frequency of the applied signal and the respective sensitivity can be found for each microcantilever used. The sensitivity corresponds to the slope of the graph of displacement as a function of the magnetic field, and is given in picometer per oersted. $M1$ presented the highest sensitivity of $(53 \pm 3)\, pm/Oe$. From $M2$, which was analyzed for 3 different frequency values, it was possible to conclude that sensitivity decreased with increasing frequency. Sensitivity could not be calculated for either $M3$ nor for $M2$ at high frequencies, due to the non-linearity of the displacement curves.

microcantilever	dimensions ($\mu m \times \mu m$)	area ($\times 10^4 \mu m^2$)	frequency (Hz)	sensitivity (pm/Oe)
$M1$	30×180	0.54	1	53 ± 3
$M2$	30×60	0.18	1	4.8 ± 0.1
			5	3.7 ± 0.2
			10	1.9 ± 0.7
$M3$	100×60	0.60	1	——

Table 4.5: Dimensions (length×width) of the microcantilevers used, and respective surface areas, frequency of the applied signal, and correspondent sensitivity values.

4.2.3 Simulations

Simulations were ran in COMSOL Multiphysics software in order to compare the numerical results with the ones obtained experimentally. The simulations were planned and conducted in collaboration with Tiago Ferreira, a colleague doing his Master's degree in

Physics Engineering in the Faculty of Sciences, University of Porto. This software allowed the modification of multiple geometrical and physical parameters to better simulate the actual scenario. A SiO_2 substrate with a deposition of a $Co_{66}Fe_{34}$ thin film was modulated. Its dimensions were chosen to coincide with those of microcantilever $M1$: $30 \times 180\,(\mu m \times \mu m)$ and a $136nm$-thick magnetostrictive film, and choosing a $20\mu m$ lateral margin between the magnetostrictive film and the substrate edge. A magnetic field was simulated to actuate parallel to the length of the cantilever, but instead of an AC magnetic field, a DC field was used. Two different simulations were run, for two different saturation magnetostrictive coefficients: $\varepsilon_{S1} = 60ppm$ and $\varepsilon_{S2} = 50ppm$, simulation 1 and 2, respectively. To approximate the simulation to reality, the chosen medium was air. The displacement as a function of the applied magnetic field is depicted in Figure 4.36, for both simulations, and for the experimental curve obtained for microcantilever $M1$.

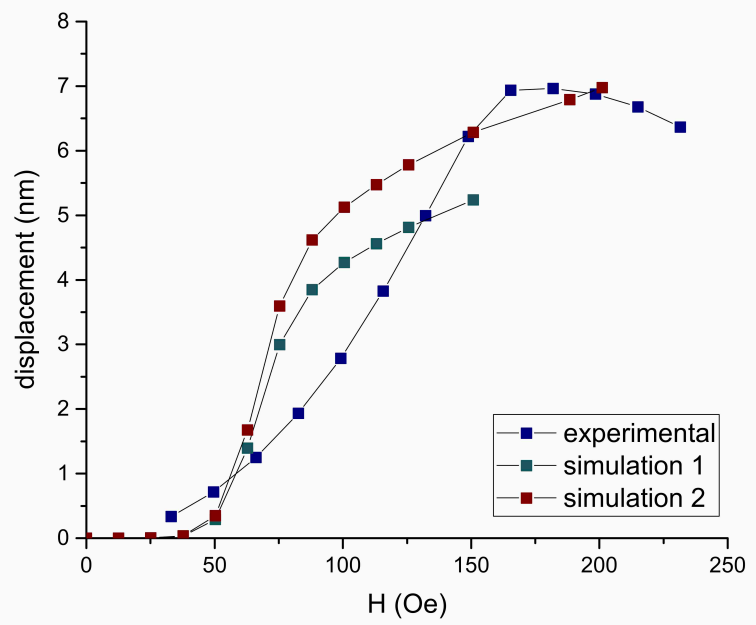

Figure 4.36: Displacement as a function of the applied magnetic field – $M1$ – experimental and simulation results.

It is possible to perceive a few similarities between the experimental data and the simulations. For the same magnetic field range, the values of displacement are of the same order. However, for both simulation signals, a threshold magnetic field is needed for the displacement to start increasing. This threshold value was not present for experimental results obtained for microcantilevers $M1$, $M2$, and $M3$, possibly due to a lack of resolution in the PSD used in the experimental setup.

When saturation is reached, around $H = 170Oe$, the displacement values obtained by

the simulations were lower than the ones obtained experimentally. The above displayed results were only preliminary tests, used to support the experimental data acquired through the optical system. However, these simulations showed that the thin films fabricated present magnetostriction and its saturation magnetostrictive coefficients are of the order of $50ppm$ or $60ppm$. These results are in the same range of values obtained in the literature: Hunter *et al.* obtained a saturation magnetostrictive coefficient $\varepsilon_S = (67 \pm 5)ppm$ for an as-deposited $0.5\mu m$ thick $Co_{66}Fe_{34}$ thin film [37], and Nakajima *et al.* obtained $\varepsilon_S = 56ppm$ for a $240nm$ thick $Co_{68}Fe_{32}$ thin film, quenched from $400\,^{\circ}C$ [4].

4.3 Discussion

A magnetostrictive $Co_{66}Fe_{34}$ thin film was deposited on a hydrogenated amorphous silicon layer and its atomic structure and magnetic properties were studied. This sample – $SiMag-r$ – showed a $Co-Fe$ crystalline phase and a ferromagnetic behavior. A $Co_{66}Fe_{34}$ thin film was then deposited on a die of microcantilevers – $McMag-r$ – under the same deposition conditions, and similar results were obtained using XRD analysis. Based on these results, a magnetostrictive behavior was expected for the thin film. In fact, following measurements showed a deflection of the microcantilevers, indicating that the thin film presented in fact a magnetostrictive response.

The optical characterization system allowed for the measuring of nanometric microcantilever displacements, with picometric sensitivity and for a magnetic field ranging from $0Oe$ to about $250Oe$. The maximum sensitivity obtained was $(53 \pm 3)\,pm/Oe$, and the saturation magnetostrictive coefficient obtained is in the range of values obtained by other authors [4, 37]. Moreover, the microcantilevers appear to relax and return to their initial position after the magnetic field is removed. This fact allows for the repetition of the experiment without damaging the microcantilevers and without compromising the results.

The measuring technique presented some downsides. Firstly, it was extremely slow, being that a single measurement for one microcantilever, at one specific frequency of the applied signal, could last for about two hours. Also, the laser used had a large spot size, which made it difficult to align the laser beam with only one microcantilever. For future work, these experiments could also be done for increasing and decreasing magnetic fields, in order to see if hysteretic behavior is present. The displacement as a function of the applied magnetic field, and for different frequencies, can also be measured for a larger number of microcantilevers, so as to relate their sensitivity with their dimensions.

This optical method has proven to be very efficient in the measuring of displacement in microcantilever, however it has already been extensively used by other authors. A novel method based on FP interferometry is herein proposed, and will be discussed in the following chapter.

Chapter V

Optical Characterization based on Fabry-Perot Interferometry

Initially, a measuring system comprised of a laser and a position sensitive photodetector was assembled to measure the displacement of microcantilevers. But as mentioned, many results using this technique can already be found in literature. For this reason, a new technique for measuring deflection of these microstructures under a magnetic field is proposed. It is based on the multi-interference of light in the small cavity, creating a FP interferometer between a taper tip and a microcantilever.

Taper Tip Preparation

The taper used to measure deflection was produced from a conventional single mode fiber *SMF28e* through CO_2 laser ablation. The fiber was clamped between two *Aerotech* translation stages which were controlled by a LabVIEW program in a computer. To ensure that the fiber was in tension, one of the translation stages was moved away from the other in steps of $2\mu m$ at a time, stretching the fiber. When the fiber was at maximum tension, without any deformation, the translation stages were programmed to move in the same direction, with velocities $3500\mu m/s$ and $45\mu m/s$. Simultaneously, a $30W$ CO_2 laser beam was focused on the fiber at 19% power, using a two mirror system to elevate the beam, and two lenses: a $100mm$-focal length plano-convex lens to focus the beam on the fiber, and a $150mm$-focal length concave lens to refocus the beam on the back of the fiber. This process was followed using a CCD imaging system connected to the computer, and suspended above the taper waist region. The fabricated taper used in this experiment had a waist diameter of $\approx 23\mu m$.

To produce a polished taper tip, the taper was broken in half in the waist region, and a focused ion beam, *FIB*, was used to mill one of the two rough taper tips created.

To prevent charge accumulation during the ion milling process, an approximately $70nm$ tantalum coating was applied to the rough taper tip. For that purpose, the taper was glued to an aluminum sample holder with a conducting silver paste, and introduced in an *EM MED020* vacuum coating system by *Leica*. This system uses an argon plasma source to sputter atoms from a Ta target, which then deposited on the taper. Using a current of $60mA$, a working pressure of $5 \times 10^{-2}mbar$, and a distance of $50mm$ between the taper and the target, the uniform coating was obtained after $100s$.

After the coating, each taper was ion milled using a *Lyra FIB-SEM* by *Tescan*. The taper was placed inside a chamber at pressure $< 9 \times 10^{-5}mbar$. Initially, the rough taper tip was placed on a holder inside the chamber, perpendicularly to the ion column. This holder was able to move in the x, y, and z directions, and also to rotate around its axis and tilt. The first cleave was performed using a large *fillet rectangle* milling pattern and a $3nA$ ion current. A milling depth approximately equal to the diameter of the taper tip was chosen, to ensure that all the material throughout the taper cross section was removed. A flat cross section was created in the taper but still with an irregular finishing. For polishing, a smaller *polish rectangle* pattern, and a lower beam current of $100pA$, were used to obtain a high resolution taper tip surface. Figure 4.37b shows a taper tip after the milling process.

Since significant optical loss can arise from the tantalum coating on the taper [71], the remaining Ta was removed introducing the taper tip in acetone and placing the container in a *Bandelin Sonorex* ultrasonic bath.

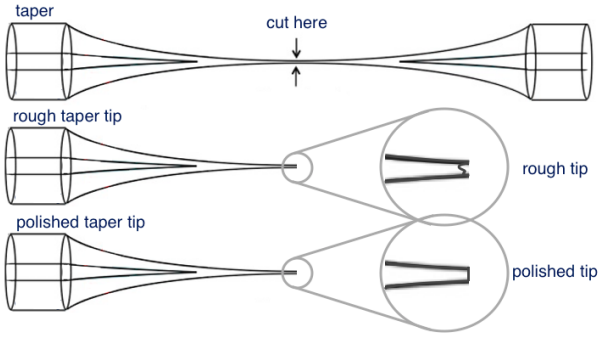

(a) Schematic of the fabrication of a polished taper tip from a taper.

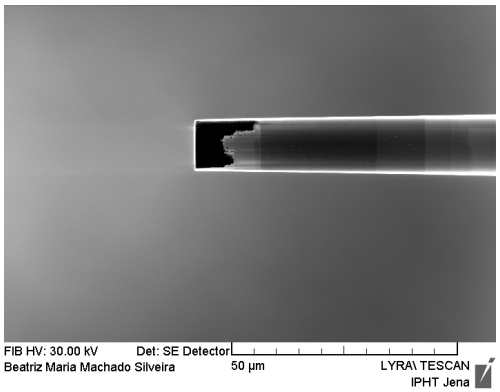

(b) Taper tip after polishing – using a small ion current; FIB imaging.

Figure 5.37: Taper tip fabrication process using FIB milling.

Magnetostrictive Microcantilever Preparation

A die of microcantilevers was fabricated in INESC-MN, in Lisboa, and the description of its fabrication is described in detail in Section 4.2 – *Microcantilever Microfabrication*. The die – sample $McMag - r$ – is comprised of 810 hydrogenated amorphous silicon microcantilevers with a magnetostrictive $Co_{66}Fe_{34}$ thin film deposition.

Experimental Setup

A broadband light source with a central wavelength of $1550nm$ and a bandwidth of $100nm$ was connected to an optical circulator. Using a single mode fiber – $SMF28e$, the light was coupled to the optical circulator, which then coupled the light into the taper. The taper was glued to a small translation stage with a manual micrometer, so the distance between the taper tip and the die of microcantilevers could be controlled. A magnifying glass was used to help aligning the taper tip with the loose end of only one microcantilever. The following image shows a taper tip near a row of microcantilevers during the alignment

process. The poor resolution of the image comes from the fact that the picture was taken through the ocular lens of a magnifying glass.

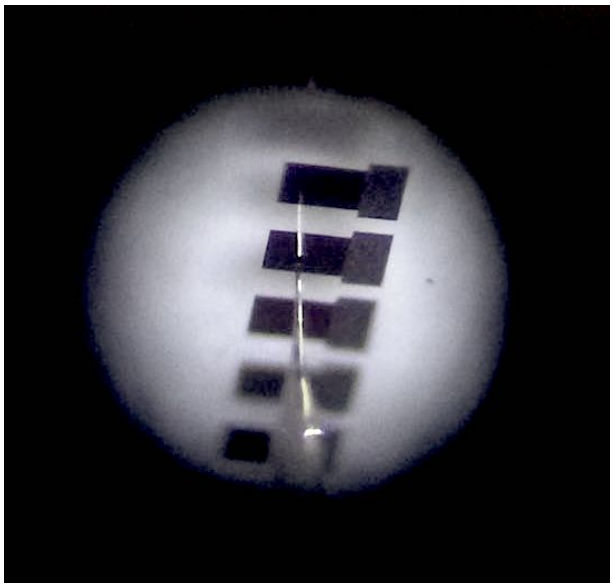

Figure 5.38: Picture of a row of microcantilevers and a taper tip, taken through the lens of a magnifying glass.

About 3.3% of the light traveling in the taper is reflected in the glass-air interface at the cleaved taper tip. This value was calculated through the Fresnel reflectivity equation for normal incidence, and assuming the refractive indexes for fiber and air to be 1.444 and 1 at $1550nm$, respectively[1]. The remaining light leaves the taper tip and is guided to the die of microcantilevers, whose surface is placed perpendicularly to the taper tip. Part of this light is reflected in the microcantilever and is guided back into the optical fiber. The resulting signal is an interference of both reflected signals – the first in the glass-air interface and the second in the microcantilever – and so this cavity behaves as a FP interferometer. The reflected signal returns to the circulator and is then directed to an optical spectrum analyzer, OSA, which was previously normalized to the reflectivity of the system with a flat cleaved $SMF28e$ optical fiber.

To actuate the magnetostrictive film deposited on the microcantilevers, a magnetic field was applied in the direction longitudinal to the thin film. Initially in this work, a small hand magnet was used to generate the magnetic field. The experimental setup was just starting to be established, so a magnet would be easier to incorporate in the system since it takes up less space and is easily adjusted to this configuration. Later on, the setup was

[1] www.refractiveindex.info

optimized, and the same experiment was repeated using a pair of Helmholtz coils. The microcantilever studied had dimensions 200×180 ($\mu m \times \mu m$). A *BOP 50-2M* Kepco was used to generate a DC electric current to supply the coils, and the die of microcantilevers was placed in the center of the coils [Figure 5.39]. The power supplied by the Kepco was increased in discreet steps of $0.5A$, until a maximum value of $2A$, and then lowered to $-2A$ to complete a cycle. By using Helmholtz coils, highly uniform fields can be achieved. Based on the magnetic field range obtained during the experiment using a laser and a PSD for measuring deflection on microcantilevers (Subsection 4.2.2 – *Optical Characterization using a Laser and PSD Configuration*), higher magnetic fields were expected. However, the same pair of Helmholtz coils could not be used, and the highest magnetic field generated was about $64.67Oe$.

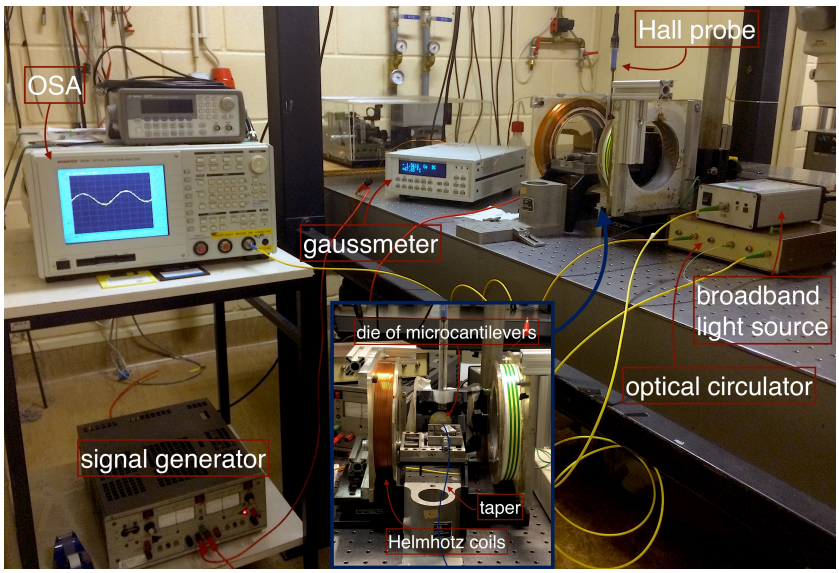

Figure 5.39: Setup of the optical characterization system based on Fabry-Perot interferometry using Helmholtz coils.

The magnetic field intensity was measured using a *Lakeshore 455 DSP* gaussmeter, connected to a Hall probe placed directly above the die of microcantilevers. The following figure shows the experimental setup.

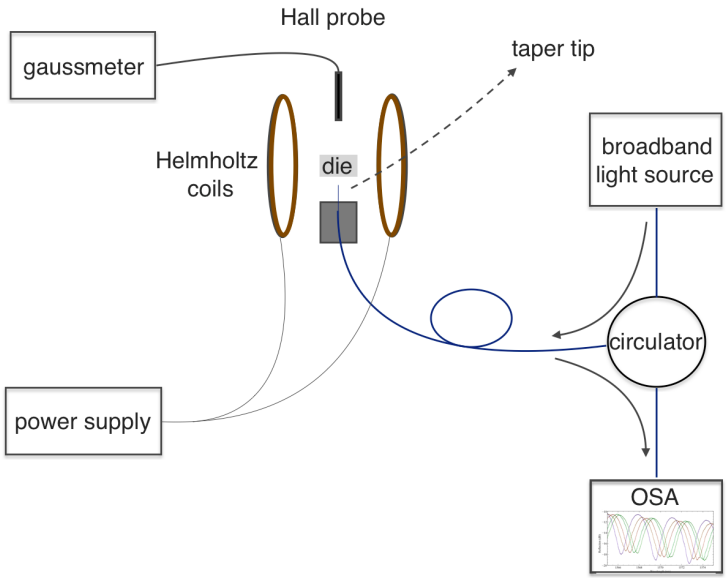

Figure 5.40: Schematic of an experimental setup based on Fabry-Perot interferometry – a light beam is reflected on a taper tip and on a microcantilever, and the resulting signal is analyzed in an OSA; a magnetic field is generated using two Helmholtz coils, inducing a magnetostrictive response in the microcantilevers.

All the equipment used in the experimental setup was assembled on an optical table to reduce vibration and increase stability in the measuring system.

Results

The magnetic field in the vicinity of the microcantilevers was varied by changing the current passing through the coils. Each time, the magnetic field intensity H was registered by the Hall probe and the optical spectrum of the reflected signal was analyzed in the OSA. The resulting optical spectra showed a signal typical of a FP structure.

The following plots show the obtained reflection spectrum in the OSA. For an increasing magnetic field [Figure 5.41a], a redshift in the spectrum is visible. Decreasing H [Figure 5.41b], a phase shift is also present, but this time in the opposite direction. Looking again at Equation 7a, it is possible to see that the phase of the signal is proportional to the cavity length, L, *i.e.* the distance between the taper tip and the microcantilever. Therefore, a redshift in the reflection spectrum can be associated with an increase in L [Figure 5.41a], while a blueshift is expected for a decreasing L [Figure 5.41b]. In this case, the cavity length corresponds to the distance between the taper tip and the microcantilever, and so an increase in L means that the cantilever is deflecting downwards, *i.e.*, in the direction opposite to the taper, and a decrease in L is associated with the relaxation of

the microcantilever to its initial position.

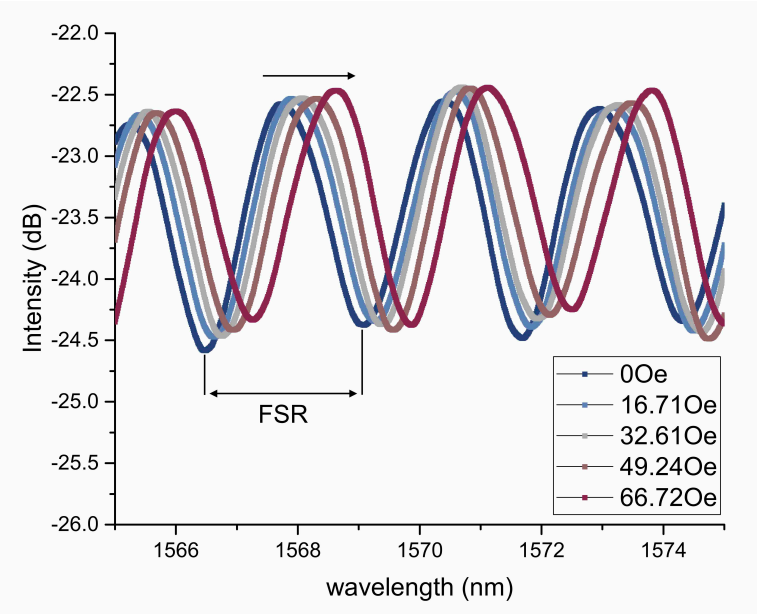

(a) Intensity of reflection for an increasing applied magnetic field.

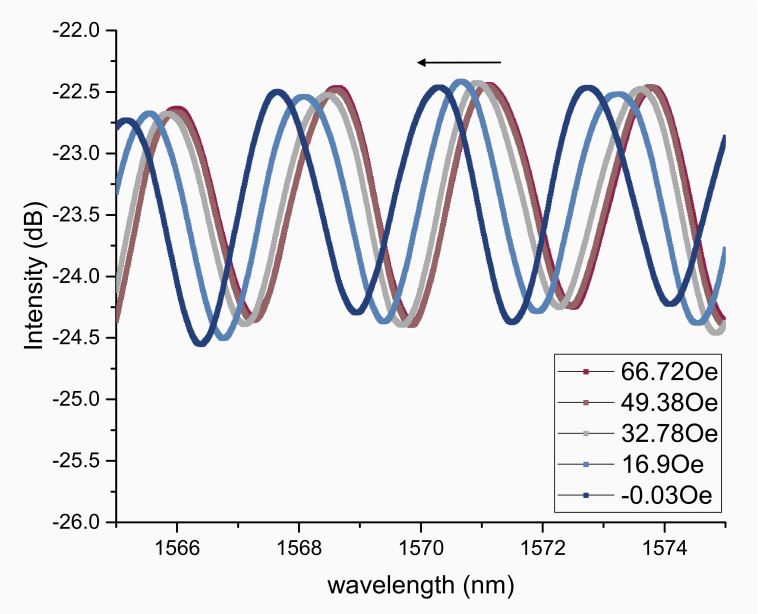

(b) Intensity of reflection for a decreasing applied magnetic field.

Figure 5.41: Reflection spectrum under a varying magnetic field.

In Figure 5.41a, the free spectral range, FSR, is signaled for a fringe in the spectrum. Using Equation 7b**,** and measuring FSR from the plots, it is possible to calculate the value of L. To easily obtain the FSR values as a function of H, the minimum peaks of the reflection spectra were tracked. The following plots show the shift of the peaks as a function of H using the coils, for both increasing and decreasing H. Again, a FSR value is signaled in Figure 5.42.

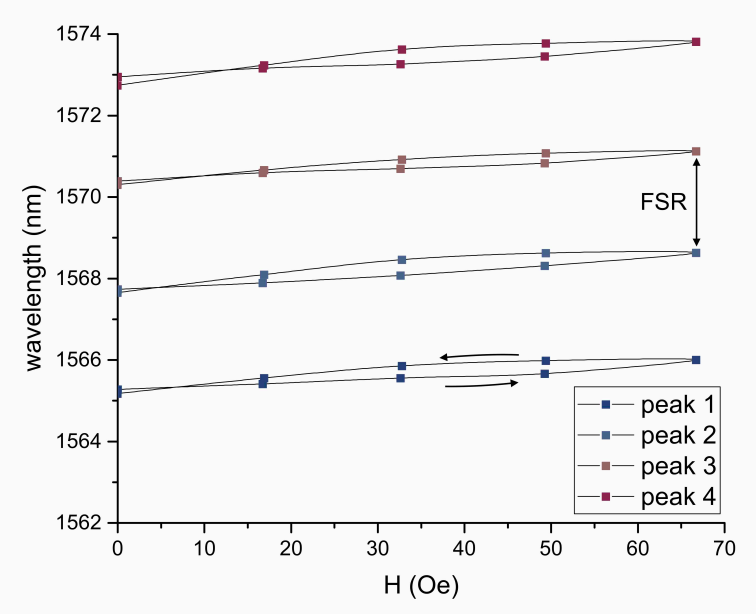

Figure 5.42: Wavelength shift of 4 peaks as a function of the applied magnetic field.

It is possible to discern a nonlinear correlation between the wavelength shift and H, and a slight hysteretic behavior between the curves for increasing and decreasing magnetic field is present. Zhang *et al.* [2] measured the elongation of a slab of $Terfenol - D$ using a fiber-optic FP interferometer under a magnetic field and, despite using a rather different configuration, a nonlinear behavior was also obtained for fields below $100Oe$. The linearity was only obtained for fields in the range from about $100Oe$ to $880Oe$.

The FSR is given by the wavelength difference between two consecutive peaks. Since four peaks were traced for each value of H [Figure 5.42], three sets of L values could be calculated [Equation7b], being the average used in further calculations. The displacement of the microcantilever corresponds to the average cavity length L, for a given H value, minus L_0. L_0 corresponds to the initial cavity length, under no applied magnetic field. The displacement of the microcantilever as a function of H is plotted.

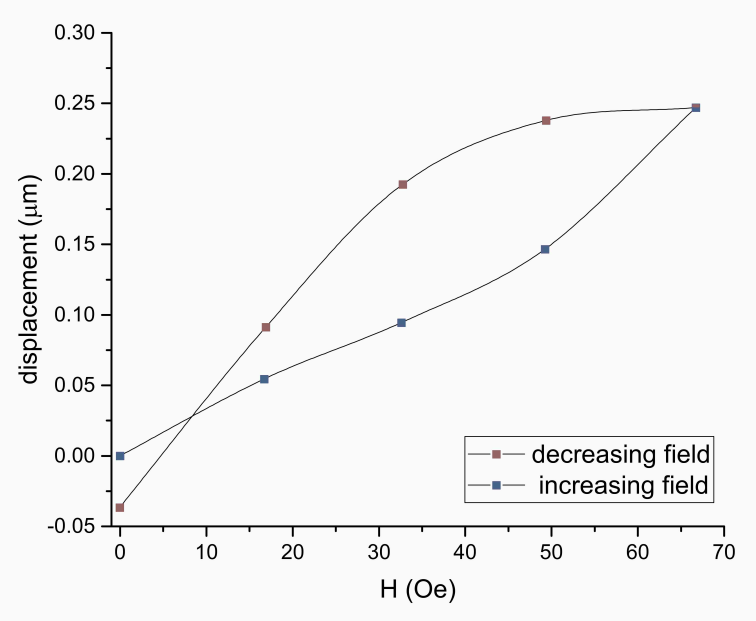

Figure 5.43: Displacement of a microcantilever as a function of the applied magnetic field.

The plot shows the displacement of the microcantilever under a magnetic field. The displacement increases with increasing H, reaching a maximum for the highest H value, as expected. Decreasing the magnetic field, the microcantilever gradually returns to its initial position and the displacement decreases. However, when H reaches zero, the displacement is not zero. The maximum measured displacement was approximately $0.25\mu m$. Since the support of the microcantilever is approximately $1.02\mu m$ high, this displacement corresponds to a deflection of the microcantilever in the direction of the substrate by a quarter of its height. The measured values of displacement seem to be too high, specially when compared to the results obtained using the above mentioned optical indirect method (Subsection 4.2.2 – *Optical Characterization using a Laser and PSD Configuration*), *i.e.*, three orders of magnitude higher. Nonetheless, the characterization system still lacks optimization, and some adjustments can be made in order to obtain more plausible results. Due to the nonlinear behavior of the curves, it was not possible to obtain the sensitivity of this sensor. However, based of the work of Zhang *et al. [2]*, a linear behavior is predicted for higher magnetic fields and the subject can be explored in the future.

5.1 Discussion

A measuring system was assembled to detect small displacements on magnetostrictive microcantilevers. For the purpose, an optical taper was used to shine light on one mi-

crocantilever and collect the reflected light. The interference of the light reflected on the taper tip and on the surface of the microcantilever was analyzed using an OSA. The magnetostrictive film on the microcantilever was actuated using a pair of Helmholtz coils fed by a DC current. The magnetic field was measured using a Hall probe connected to a gaussmeter.

By examining the reflection spectra, it was possible to discern a deflection of the microcantilever in the direction of the substrate for an increasing magnetic field, and a relaxation of the microcantilever to almost its initial state by decreasing the magnetic field to zero. From the equations for the cavity length and phase, characteristic of a Fabry-Perot interferometer, the maximum displacement was calculated and an approximately $0.25\mu m$ value was obtained. This displacement seems to be unlikely when compared to the maximum displacement obtained by the previous method. For the magnetic field range used, the peak wavelength shift was not linear, which is in agreement with a similar experiment based on FP interferometry found in literature [2].

In summary, this optical characterization system could be used as an alternative method for detecting and measuring displacements in microcantilevers. However, the setup still lacks stability, and optimization is required to obtain better results. Furthermore, the system appeared to be very sensitive to external stimuli, such as touching the optical table, airflow, and even footsteps, which could compromise the quality of the results. A way to overcome the problem, or at least reduce it, would be to setup the taper and the die of microcantilevers on top of a single structure. That way, a vibration in the system would lead to a displacement of both structures in the same fashion. Additionally, the measuring system could be enclosed to avoid airflows. In the future, a study will be made for higher applied magnetic fields and for multiple microcantilevers with different dimensions.

Chapter VI

Novel Taper Tip Configurations based on Fabry-Perot Interferometry

In the previous chapter, a new technique for measuring deflection in microcantilevers was described. However, as mentioned before, a good alignment between the taper tip and a single microcantilever was difficult to achieve, due to the small dimensions of both structures. To reduce optical losses which arise from small misalignments, two different structures were developed to potentially replace the flat-top taper tip used during the measurements. These new sensors were again fabricated through tapering and FIB milling.

Initially, single-mode $SMF28e$ optical fibers were tapered down to a few micrometers in diameter, using CO_2 laser ablation or the Ring of Fire. The tapers were then broken in half to make two taper tips, which were sputter coated with an approximately $70nm$ tantalum layer. After the coating, the taper tips were introduced in a FIB chamber, one at a time, to produce the desired taper tip structures.

The parameters used for tapering, coating, and milling are similar to the ones used in the previous chapter for the fabrication of a flat-top taper tip. A taper tip is the starting point for the fabrication of the following structures.

6.1 Angled Taper Tip

When a flat-top taper tip was used to measure deflection of a microcantilever, the taper tip was horizontally suspended on air in proximity to the microcantilever. Small instabilities in the system can cause the taper to slightly move, leading to the deviation of light away from the microcantilever, and consequently leading to optical power losses. A possible solution would be to hold the taper and the microcantilever together, with the taper parallel to the longitudinal direction of the magnetostrictive film, in a way that the taper wouldn't be

hanging. This solution seems to solve the instability problem, but installs another one: if the taper is placed parallel to the film, light traveling the optical fiber will leave the taper tip but won't be reflected in the microcantilever. The problem can be solved if instead of a flat-top taper tip, the taper tip is cleaved with an angle. Light traveling through the optical fiber is reflected in the glass-air interface, but in this case the angle of incidence is other than 90°. According to Fresnel's law of reflection, $\theta_i = \theta_r$, the incident light beam on the interface will be reflected at the same angle. Thus, if the taper tip is cleaved at an angle equal to 45°, the reflected beam will be perpendicular to the incident beam and will be directed towards the microcantilever [Figure 6.44b]. The critical angle, angle above which all light is reflected, can be calculated using Snell's law:

$$n_{fiber} \sin\theta_i = n_{air} \sin\theta_t \Longrightarrow n_{fiber} \sin\theta_c = n_{air}, \tag{8}$$

where n_{fiber} and n_{air} are the refractive indexes of the optical fiber and air, respectively, θ_i is the incident angle, and θ_t is the transmission angle with respect to the normal of the surface. For a taper with a refractive index of $1.444@1550nm$ in air, the critical angle is approximately $\theta_c = 43.83^\circ$. Since the incident angle is higher than the critical angle, $\theta_i > \theta_c$, there is no transmission of light and all incident light is directed downwards. Light is then reflected on the glass-air interface and on the surface of the microcantilever [Figure 6.44c]. There is interference of both signals and the resulting reflection spectrum will again be the typical fringe spectrum expected for a FP cavity.

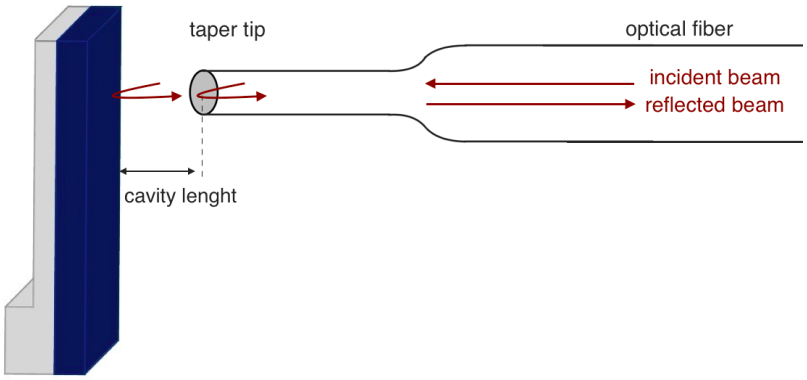

(a) Taper tip placed perpendicularly to the magnetostrictive microcantilever.

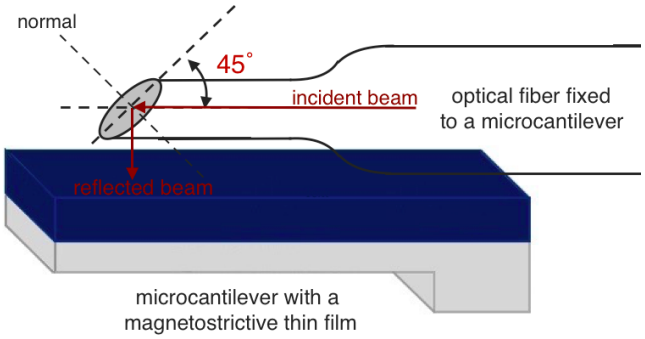

(b) Reflection of light in a taper tip cleaved at 45 °, placed parallel to the magnetostrictive microcantilever. No light is transmitted due to the high angle of incidence.

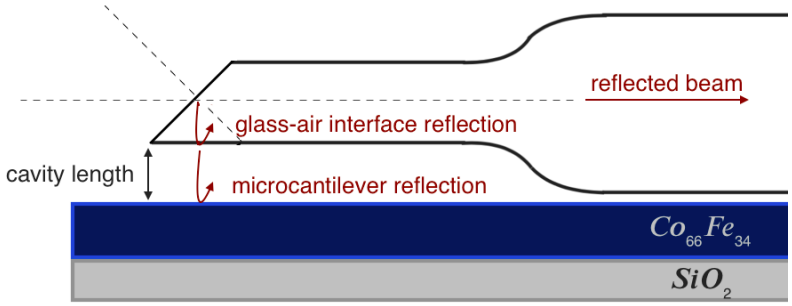

(c) Light reflections that contribute to the interferometer.

Figure 6.44: Schematic of an angled taper tip as a deflection sensor.

The fabrication of the cleaved taper tip was performed using a focused ion beam. The milling process is similar to the one used for the fabrication of a flat-top taper tip, except that after the tip is created, a *fillet rectangle* milling pattern and a $2nA$ ion current were used to cleave the tip at a 45 ° angle. The procedure was undertaken in various steps, milling small patterns one at a time [Figure 6.45a]. The finishing pattern, *polish rectangle* pattern, was narrower and milled with a lower current, $100pA$, to achieve a high resolution

surface. Two views of one of the angled taper tips obtained are shown in Figures 6.45b and 6.45c.

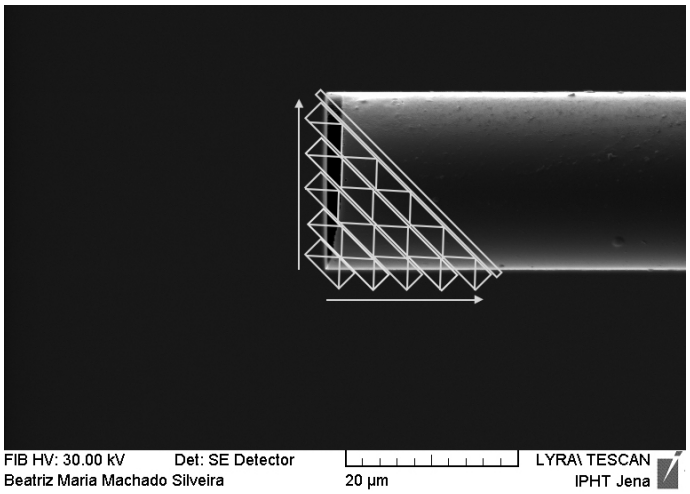

(a) Oblique *fillet rectangle* milling patterns for the fabrication of 45 ° angle cleaved tips.

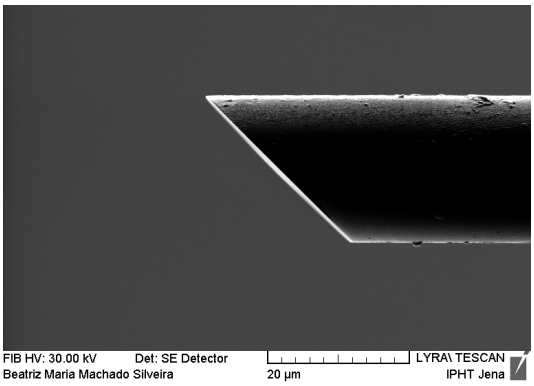

(b) Lateral view of the resulting angled taper tip.

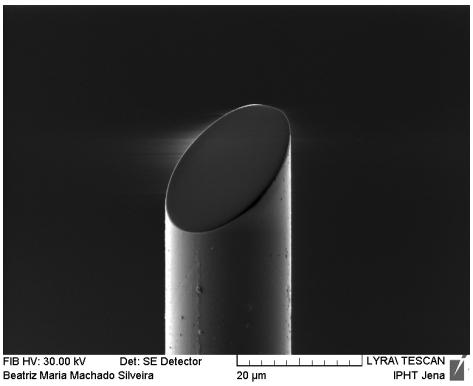

(c) Rotated view of the resulting angled taper tip. From this perspective it is possible to discern a very polished surface in the tip.

Figure 6.45: Angled taper tip fabricated using ion milling – FIB imaging.

The structures fabricated were not yet tested or used for measuring deflection in microcantilevers, but will be in the future. By attaching the taper tip and the microcantilever together in the measuring system, a higher stability is expected, therefore diminishing optical losses.

6.2 Microcantilever Structure on a Taper Tip

A second structure was developed to try to reduce misalignment and optical power losses. A possible solution is to combine the taper and the microcantilever in the same structure, in order to avoid displacements of the taper during measurements. The second design

proposed is an all-fiber taper microcantilever.

The sensor was fabricated by milling a cantilever in a taper near its tip, creating an air cavity. When light is coupled in the optical fiber, light will travel through the taper and will be reflected when it reaches an interface. In this case, light will not only be reflected in the taper tip, but also in interfaces 1 and 2 [Figure 6.46]. In the reflection spectrum, the contribution of three different cavities are expected to be present, one for each pair of reflecting interfaces:

1. air cavity – between interfaces 1 and 2;
2. silica cavity – between interface 2 and the taper tip;
3. silica and air cavity – between interface 1 and the taper tip.

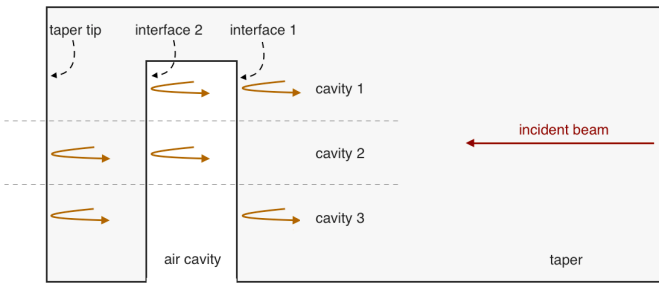

Figure 6.46: Schematic of an all-fiber taper microcantilever. When light travels through the taper, light is reflected on the multiple interfaces. The interference of each two reflections gives information about a different optical cavity.

However, it might be difficult to distinguish between the multiple cavities through the reflection spectrum. A way to get around the problem is to fast Fourier transform the spectrum. Fourier analysis allows for the demultiplexing of the unprocessed data into separated signals. 3 different peaks are expected to be visible in the resulting spectrum, one for each cavity. The optical path of each cavity can be extracted from the spectrum, and a change in the optical path can be measured through a shift of one of the peaks [72].

Depositing a magnetostrictive thin film on the surface of the taper tip, *i.e.*, on top of the microcantilever, the sensor will be sensitive to an external magnetic field. Similarly to what occurs in a die of microcantilevers, if a magnetic field is applied to this all-taper sensor, the elongation of the magnetostrictive film will cause the microcantilever to bend, changing the length of the $1st$ cavity (air cavity). The magnetostrictive film induces additional reflections of light near the taper tip:

4. silica, air, and magnetostrictive film cavity – between interface 1 and the film surface;

5. magnetostrictive film cavity – between the taper tip and the film surface;

6. silica and magnetostrictive film cavity – between interface 2 and the film surface.

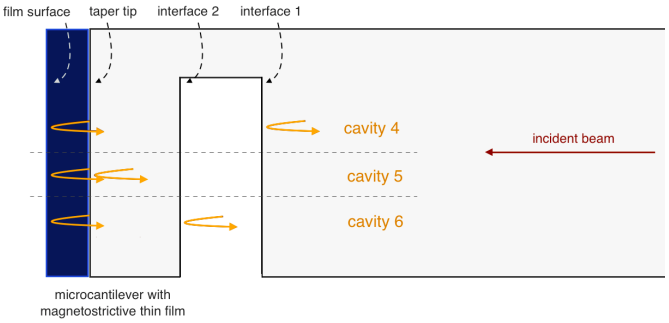

Figure 6.47: Schematic of a magnetically sensitive all-fiber taper microcantilever, with a deposition of a magnetostrictive thin film.

The deflection of the microcantilever can be measured by comparing the position of the interference peaks in the Fourier domain spectra, before and after the magnetic field is applied. The peaks expected to change are the ones associated with a cavity that comprises the air cavity, *i.e.*, cavities 1, 3 and 4 [Figures 6.46 and 6.47]. The peak shift can be converted into a cavity length change, which corresponds to the value of deflection of the microcantilever.

The fabrication of the microcantilever near the taper tip was performed through ion milling. Initially, a flat-top taper tip was fabricated following the procedure already described in a previous section – *Taper Tip Preparation*. To create the microcantilever, a *fillet rectangle* milling pattern and a $2nA$ ion current were used to mill a cavity in the taper, approximately $10\mu m$ away from the taper tip. The pattern was drawn with a lower length than the taper diameter, since the milling process shouldn't cleave the whole taper section [Figure 6.48a – arrowed pattern]. The finishing of the inner surfaces was achieved using a *polish rectangle* pattern and a $100pA$ current [Figure 6.48a – bold edges]. Figures 6.48b and 6.48c show an example of a microcantilever fabricated using this process.

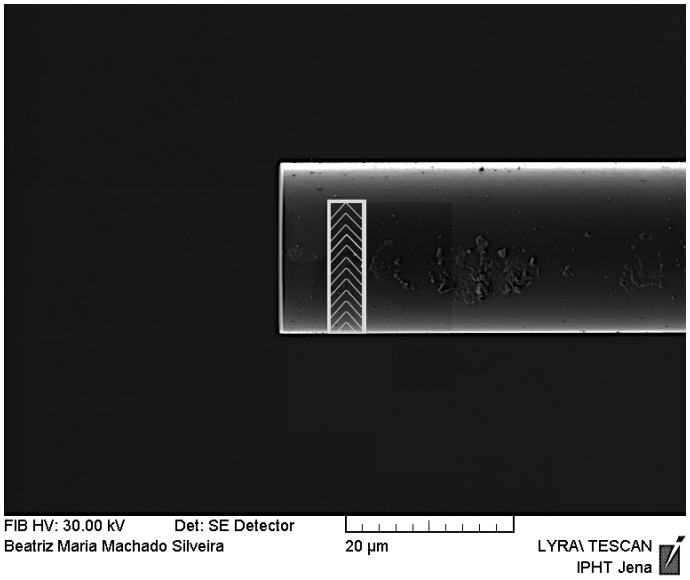

(a) Milling patterns used to mill a microcantilever near a taper tip.

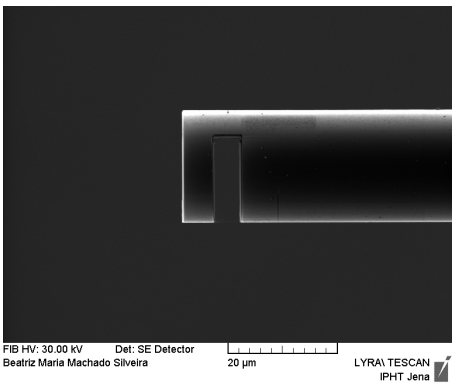

(b) Lateral view of the microcantilever near a taper tip.

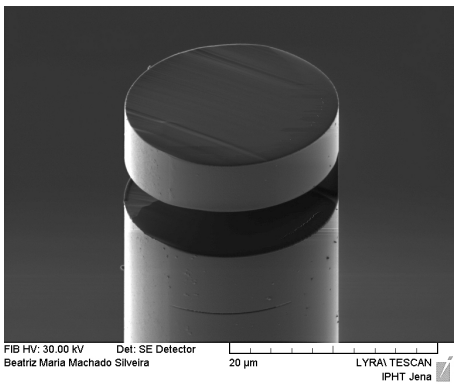

(c) Vertical and tilted view of the structure.

Figure 6.48: Microcantilever structure on a taper tip, fabricated using ion milling – FIB imaging.

The sensor is still being developed, and so it was not yet tested. Although the taper structure is already prepared, a magnetostrictive thin film still needs to be deposited. For that, EBPVD will be used to evaporate a $Co_{66}Fe_{34}$ thin layer on the surface of the microcantilever. The thickness of the film, the distance between the cavity and the taper tip, and the cavity length still need to be tuned and optimized, in order to obtain a good deflection sensitivity.

6.3 Discussion

In the previous chapter – *Optical Characterization based on Fabry-Perot Interferometry*, an optical method for measuring deflection in microcantilevers was described. Although the

method appeared to be successful in measuring small microcantilever displacements, optical losses can arise from small misalignments between the taper tip and the microcantilever. In order to increase stability of the system, two new optical configurations were proposed, and two sensors were fabricated, which will be tested in the future.

In the first configuration, an angled taper is connected to the microcantilever, which in principle will reduce deviations of the taper tip. The method relies on total internal reflection of light, since the beam traveling through the taper is reflected on its tip at an angle higher than the critical angle.

The second configuration is an all-fiber sensor, comprised of a magnetostrictive microcantilever milled directly near a taper tip. The main advantage of this sensor is that a die of microcantilevers will not be needed, since the microcantilever is itself part of the taper.

These sensors take more time to produce and require a more detailed fabrication than flat-top taper tips. However, during experiments, time is expected to be saved because there is no need for thorough alignments in the measuring system.

Chapter VII

Conclusions and Future Work

In this Master's dissertation, the detection and measurement of deflection in microcantilevers under a magnetic field was proposed. The deflection is based on the magnetostrictive effect found in all ferromagnetic materials.

A $Co_{66}Fe_{34}$ thin film was deposited by e-beam evaporation on a die of microcantilevers – sample $McMag - r$ – in small time intervals of 3 minutes, and in a total of 72 minutes. The sample was later characterized using XRD, and the results were compared to the ones obtained for a $Co_{66}Fe_{34}$ thin film deposited on a hydrogenated amorphous silicon layer – sample $SiMag - r$ – under the same conditions and using the same deposition parameters. Through SQUID analysis, only traces of a crystalline phase were found for both samples, being that a $99wt\%$ of the sample was estimated to be amorphous. For further crystallization, the sample could go through an annealing process. This thermal treatment will be likely done in the future.

The deflection of the magnetostrictive microcantilevers was initially measured using an indirect optical characterization method. This system uses a laser, a position sensitive photodetector, a pair of Helmholtz coils, and a PZT for calibration. The curve of displacement of the microcantilevers as a function of magnetic field was expected: initially, the displacement of the microcantilevers increased almost linearly, corresponding to the reorientation of the magnetic domains in the direction of the magnetic field, reaching a saturation later on, when the domains were all oriented in the same direction. Sensitivities in the order of picometers were obtained in a range from $0Oe$ to about $160Oe$. The experiment demonstrated high repeatability, which is also an indication that the microcantilevers weren't damaged for fields lower than $250Oe$. Simulations performed in COMSOL are in agreement with the obtained experimental results. This software will be further explored, and the deflection of a microcantilever will be studied for a wider range of parameters.

Comparing the experimental results with the simulations, a saturation magnetostrictive coefficient in the order of $50ppm$ or $60ppm$ can be estimated for our sample. These values are in agreement with the ones obtained for pure crystalline alloys by Hunter *et al.* – $\varepsilon_S = (67 \pm 5)ppm$ for an as-deposited $0.5\mu m$ thick $Co_{66}Fe_{34}$ thin film [37] – and Nakajima *et al.* – $\varepsilon_S = 56ppm$ for a $240nm$ thick $Co_{68}Fe_{32}$ thin film, quenched from $400\,^{\circ}C$ [4]. These results indicate that, even for highly amorphous samples, the magnetostrictive effect can be present.

Optical tapers were fabricated using three different techniques: CO_2 laser ablation, Vyctran, and Ring of Fire technology, allowing for high resolution taper profiles. Flat-top taper tips were then produced through FIB milling. These taper tips were incorporated in a new optical characterization system based on FP interferometry, assembled to measure deflection in microcantilevers. This characterization technique presents some advantages over other deflection sensing methods, since the technique is non-invasive and allows for the reutilization of the sensors. The magnetic field was applied using a pair of magnetic coils and good results were obtained. Through the light reflection spectrum, it was possible to discern a deflection of the microcantilever in the direction of the substrate for increasing H, and a relaxation of the microcantilever for decreasing H. Through the equations of a Fabry-Perot cavity, a maximum displacement of $0.25\mu m$ was measured for a magnetic field of approximately $70Oe$. The viability of using optical taper tips to measure small displacements was demonstrated. Despite being only preliminary tests, very promising results were obtained with this novel technique. The experiment will be repeated in the future and better sensitivities are expected with further system optimizations.

To increase stability in the previous experimental setup, two new structures were fabricated with FIB milling in taper tips. One of the structures is a taper tip cleaved with a $45\,^{\circ}$ angle, that will be placed in a direction parallel to the magnetostrictive film and longitudinal to the microcantilever. The second structure is a taper tip comprising the microcantilever itself. On the surface of the microcantilever, a $Co_{66}Fe_{34}$ thin film will be deposited so it can be magnetically actuated. This all-taper sensor seems to be very promising, since it integrates the magnetostrictive microcantilever and the sensing element in one structure. Moreover, the sensor can be easily modified to achieve different resolutions by changing the height of the microcantilever (which corresponds to the cavity length), using FIB milling. Both structures were already fabricated and will be tested in future experiments.

There are only a few references on the combination of optical fiber sensors and magnetostrictive sensors, and therefore a lot more work can be developed around the topic. To deeper explore it, some points will be considered in the future:

- Investigation on the possibility of annealing on the die of microcantilevers – sample $McMag - r$, and later characterization using the FP interferometer configuration;
- Through the characterization system based on FP interferometry, measure deflection on more microcantilevers with different dimensions, and for a higher range of applied magnetic field;
- Characterization of the taper cleaved at a 45 $^\circ$ angle to evaluate its spectral stability;
- Deposition of a $Co_{66}Fe_{34}$ thin film on the surface of the microcantilever structure, milled directly on a taper tip; characterization of the sensor with subsequent modeling and optimization of the microcantilever and film dimensions, to increase sensitivity to magnetic fields;
- Study and development of new tapers for measuring magnetic field gradients.

A Runsheet

(next page)

Runsheet: MAG CANT 1

Responsible: Rui M. R. Pinto
João Belo (FCUP)

Dies produced with this runsheet:

- MAG CANT (4 dies)

---

1. Substrate Cleaning

Date: 2016/01/18

Substrate: Corning Glass (1737), 0.7 mm-thick. (2 substrates)
Equipment: Wet Bench.
Cleaning Procedure:

1 – Rinse and rub with acetone and then IPA.
2 – Alconox (30 min, sonication, 65 ºC).
3 – DI Water (30 min, sonication, 65 ºC).
4 – Rinse with IPA.
5 – Wash abundantly with DI Water.
6 – Blow dry with compressed air.

---

2. Sputtering of the Al Sacrificial Layer

Date: 2016/01/18

Equipment: Nordiko 7000 Magnetron Sputtering System
Al Thickness: 10000 Å
Recipe: 1 µm Al

Sequence:

Step	Module and Function	Description
1	Mod 4 Function 3	0.5 µm Al: 130 s
2	Mod 4 Function 6	Cooling step: 340 s
3	Mod 4 Function 3	0.5 µm Al: 130 s

Conditions:

P = 2 kW
V = 400 V
I = 5 A

Ar flow = 50 sccm
N_2 flow = 0 sccm
Pressure = 3 mTorr

Thickness measured on profilometer: 10577 Å; 10094 Å; 9853 Å = **10174 Å ± 369 Å**

---

3. Vapor Prime

Date: 2016/01/18

Coating of the sample with HDMS, which promotes photoresist adhesion.

Equipment: HDMS Oven.

Step	Conditions
Wafer Dehydration	Vacuum, 10 Torr, 2 min. N_2 inlet, 760 Torr, 3 min. Heating to 130ºC
HDMS Priming	Vacuum, 1 Torr, 3 min. HDMS, 6 Torr, 5 min.
HDMS Exhaustion	Vacuum, 4 Torr, 1 min. N_2 inlet, 500 Torr, 2 min. Vacuum, 4 Torr, 2 min.
Pressure Equalization	N_2 inlet, 3 min.

---

4. Photoresist Spin Coating

Date: 2016/01/18

Equipment: SVG Track.
Photoresist: JSR Micro PFR 7790G-27cP (Positive Photoresist).
Coater Track Programs:
Spinner Program: 6.
Oven Program: 2.
Photoresist Thickness: 1.5 µm.

Step	Description	Conditions
1	Dispense photoresist	Spinning: 800 rpm. Acceleration: 10 krpm/s. Duration: 5 sec.
2	Spin	Spinning: 800 rpm. Acceleration: 10 krpm/s. Duration: 5 sec.
3	Spin	Spinning: 2800 rpm. Acceleration: 50 krpm/s. Duration: 40 sec.
4	Spin	Spinning: 1500 rpm. Acceleration: 50 krpm/s. Duration: 10 sec
5	Hard bake	Temperature: 85 ºC. Duration: 60 sec.

5. Laser Exposure: Sacrificial Layer Definition

Date: 2016/01/18

Equipment: DWL
AUTOCAD Mask: mag_cant_1.dwg
Layer: SACRIFICIAL LAYER
DWL Files: rmrp_mag_cant_1
Map: rmrp_mag
Origin point relative to bottom left of substrate: (5000 um, 5000 um)
Focus: -20
Energy: 80
Xoff = -285 - 6.2 um
Yoff = -150 - 3.9 um
Exposure time: 10 min/die

Note: Mask converted to do etching, not liftoff.

6. Photoresist Development

Date: 2016/01/18

Equipment: SVG Track.
Developer: JSR Micro TMA 238 WA
Developer Track Programs:
Oven Program: 6.
Spinner Program: 2.

Step	Description	Conditions
1	Post exposure bake	Temperature: 110 ºC. Duration: 60 sec
2	Cool down	Duration: 30 sec
3	Rinse	Spinning: 500 rpm. Acceleration: 10 krpm/s. Duration: 5 sec.
4	Spray developer	Spinning: 500 rpm. Acceleration: 10 krpm/s. Duration: 5 sec.
5	Development	Spinning: 0 rpm. Acceleration: 10 krpm/s. Duration: 60 sec.
6	Rinse	Spinning: 500 rpm. Acceleration: 5 krpm/s. Duration: 15 sec.
7	Spin dry	Spinning: 2000 rpm. Acceleration: 10 krpm/s. Duration: 30 sec.

7. Wet Etching of the Al Sacrificial Layer

Date: 2016/01/18

Equipment: Wet bench
Etchant: Gravure Aluminium Etchant Micropur MOS (Technic, France)
LOT: 017217
Etching depth: 1000 nm
Time: 17 min
Temperature: Ambient temperature (22 ºC)
Agitation: ~500 rpm

---

8. Resist Strip

Date: 2016/01/18

Equipment: Wet Bench.
Solution: Acetone
Temperature: 22 ºC (Ambient Temperature)
Agitation: Manual

NOTE: Wash the sample to remove the photoresist, using plenty of acetone. Then, wash with DI Water, IPA, water and blow dry.

---

9. n^+ a-Si:H Structural Layer PECVD Deposition

Date: 2016/01/19

Equipment: PECVD
a-Si:H Thickness: 10000 Å
Deposition Conditions:

RF Power:	25	W
Pressure:	0.5	Torr
Substrate Temp.:	175	ºC
SiH_4 Flow:	10	sccm
H_2 Flow:	19	sccm
PH_3 Flow:	5	sccm
Time:	90	min

Example:

Thickness: 1.5 µm (Last MEMS Michael Deposition)
Time: 2 h, 15 min = 135 min (Deposition rate: 11.1 nm/min)

Parameters:

RF Power:	25	W
Pressure:	0.5	Torr
Temp. Substrate:	175	ºC
Flow (SiH_4):	10	sccm
Flow (H_2):	19	sccm
Flow (PH_3):	5	sccm

Thickness Measured on Profilometer (stack with Al sac. Layer)**:** 18183 Å; 18278 Å; 18260 Å; 18524 Å; 19952 Å
Silicon thickness (Al thickness subtracted): **8465 Å ± 745 Å**

---

10. Vapor Prime

Date: 2016/01/19

Coating of the sample with HDMS, which promotes photoresist adhesion.

Equipment: HDMS Oven.

---

11. Photoresist Spin Coating

Date: 2016/01/19

Equipment: SVG Track.
Photoresist: JSR Micro PFR 7790G-27cP (Positive Photoresist).
Coater Track Programs:
Spinner Program: 6.
Oven Program: 2.
Photoresist Thickness: 1.5 µm.

---

12. Laser Exposure: Structural Layer Definition

Date: 2016/01/19

Equipment: DWL
AUTOCAD Mask: mag_cant_1.dwg
Layer: STRUCTURAL LAYER
DWL Files: rmrp_mag_cant_2
Map: rmrp_mag
Focus: -20
Energy: 80
Xoff = -285 - 6.2 um
Yoff = -150 - 3.9 um
Exposure time: 10 min/die

Note: Mask converted to do etching, not liftoff.

---

13. Photoresist Development

Date: 2016/01/19

Equipment: SVG Track.
Developer: JSR Micro TMA 238 WA
Developer Track Programs:
Oven Program: 6.
Spinner Program: 2.

---

14. RIE Patterning of the Structural a-Si:H Layer

Date: 2016/01/19

Equipment: LAM Research Rainbow Plasma Etcher
Etch Depth: 1.0 µm
Time: 350 s
Recipe: SF_6 + CHF_3

Parameters:

RF Power:	200 W		
Pressure	100 mTorr		
ElectrodeTemperature	40 ºC	**SF_6 Flow**	50 sccm
Substrate Temperature	1 ºC	**CHF_3 Flow**	50 sccm

---

15. Resist Strip

Date: 2016/01/19

Equipment: Wet Bench.
Solution: Acetone
Temperature: 22 ºC (Ambient Temperature)
Agitation: Manual

NOTE: Wash the sample to remove the photoresist, using plenty of acetone. Then, wash with DI Water, IPA, water and blow dry.

---

16. Vapor Prime

Date: 2016/01/20

Coating of the sample with HDMS, which promotes photoresist adhesion.

Equipment: HDMS Oven.

---

17. Photoresist Spin Coating

Date: 2016/01/20

Equipment: SVG Track.
Photoresist: JSR Micro PFR 7790G-27cP (Positive Photoresist).
Coater Track Programs:
Spinner Program: 6.
Oven Program: 2.
Photoresist Thickness: 1.5 µm.

---

18. Laser Exposure: Magnetostrictive Layer Definition

Date: 2016/01/20

Equipment: DWL
AUTOCAD Mask: mag_cant_1.dwg
Layer: MAGNETOSTRICTIVE LAYER
DWL Files: rmrp_mag_cant_3
Map: rmrp_mag
Focus: -20
Energy: 80
Xoff = -285 - 6.2 um
Yoff = -150 - 3.9 um
Exposure time: 10 min/die

Note: Mask converted to do liftoff, not etching.

---

19. Photoresist Development

Date: 2016/01/20

Equipment: SVG Track.
Developer: JSR Micro TMA 238 WA
Developer Track Programs:
Oven Program: 6.
Spinner Program: 2.

---

20. Dicing: Cut Sample Into Individual Dies

Date: 2016/01/20

Equipment: Disco DAD 321 Dicing Saw
Blade Thichness (cut width) ~ 200 µm
Blade Speed: 30 000 rpm
Cutting Speed: 1 mm/s

Cutting dimensions: Channel 1 = 15.2 mm; Channel 2 = 20.2 mm

Note: After cutting, wash the dies with pressurized water but NO IPA NOR ACETONE!!!.

---

21. Magnetostricitive Film Deposition

CoFe Film Thickness: 200 nm

---

22. Magnetostrictive Film Liftoff

Date: 2016/03/17

Equipment: Wet Bench.
Microstrip: Fujifilm Microstrip 3001, LOT N4D13NAS (Or other)
Temperature: 65 ºC
Sonication: Continuous (if the magnetostrictive films adhere well)
Liftoff duration: 3 h (Until all the undesired film has came off)

NOTE: Exchange the microstrip near the end of the liftoff for a cleaner result. After release, wash with IPA, water and dry.

---

23. Photoresist Spin Coating

Date: 2016/03/17

Equipment: SVG Track.
Photoresist: JSR Micro PFR 7790G-27cP (Positive Photoresist).
Coater Track Programs:
Spinner Program: 6.
Oven Program: 2.
Photoresist Thickness: 1.5 µm.

---

24. Laser Exposure: Photoresist Mask Definition

Date: 2016/03/17

Equipment: DWL
AUTOCAD Mask: mag_cant_1.dwg
Layer: STRUCTURAL LAYER
DWL Files: rmrp_mag_cant_2
Map: rmrp_mag
Focus: -20
Energy: 80
Xoff = -285 - 6.2 um?
Yoff = -150 - 3.9 um?
Exposure time: 10 min/die

Note: Mask converted to do etching, not liftoff.

---

25. Photoresist Development

Date: 2016/03/17

Equipment: SVG Track.
Developer: JSR Micro TMA 238 WA
Developer Track Programs:
Oven Program: 6.
Spinner Program: 2.

---

26. Cantilever Release

Date: 2016/03/18

Equipment: Wetbench, apron, googles, face protection and chemical protection gloves.
Etchant: Gravure Aluminium Etchant Micropur MOS (Technic, France)
LOT: 017217
Etching depth: 45 µm (the largest width of the cantilevers divided by 2)
Time: 70 Min (depends on the structures) (calibrate time for the etchant in use: 1 µm/min)
Temperature: 60 ºC

Agitation: ~500 rpm (or periodic manual agitation)
Procedure:

1. Clean the beaker you are going to use and dispense the Al etchant. Heat up if necessary.
2. Put your sample in the etchant with the structures facing UP and start counting the time (Use acid resistant tweezers if available or wash the metal tweezers immediately).
3. When the etch time is reaching the end, clean 4 more beakers and fill them with DI Water, acetone, IPA and n-hexane, respectively.
4. Take your sample out of the etchant and, without letting it dry, put it in water for some time to wash all the acid (5 to 10 min). Then, change to acetone for a few minutes, having the same precaution (do not let the surface of the die dry!). Then, transfer to IPA, n-hexane and finally **let dry at ambient temperature without blowing. The structures are now released!**

The sequence is:

Al Etchant -> Water -> Acetone -> IPA -> n-hexane -> Dry

Don't let the samples dry when exchanging from liquid to liquid.

Alignment Mark Information for Lithography:

Bottom Alignment Marks:

Left Alignment Mark Coordinates: (285; 150) um
Distance to Right Alignment Mark: 19465 um

Top Alignment Marks:

Left Alignment Mark Coordinates: (285; 14850) um
Distance to Right Alignment Mark: 19465 um

References

[1] T. A. Birks and Y. W. Li, "The Shape of Fiber Tapers," *Journal of Lightwave Technology*, vol. 10, no. 4, pp. 432–438, 1992.

[2] P. Zhang, M. Tang, F. Gao, B. Zhu, S. Fu, J. Ouyang, Z. Zhao, H. Wei, J. Li, P. P. Shum, and D. Liu, "An Ultra-Sensitive Magnetic Field Sensor Based on Extrinsic Fiber-Optic Fabry-Perot Interferometer and Terfenol-D," *Journal of Lightwave Technology*, vol. 33, no. 15, pp. 3332–3337, 2015.

[3] M. Ali and R. Watts, "Measurement of saturation magnetostriction using novel strained substrate techniques and the control of the magnetic anisotropy," *Journal of Magnetism and Magnetic Materials*, vol. 202, no. 1, pp. 85–94, 1999.

[4] T. Nakajima, T. Takeuchi, I. Yuito, K. Kato, M. Saito, K. Abe, T. Sasaki, T. Sekiguchi, and S.-i. Yamaura, "Effect of Annealing on Magnetostrictive Properties of Fe- Co Alloy Thin Films," *Materials Transactions*, vol. 55, no. 3, pp. 556–560, 2014.

[5] Z.-Y. Cheng, S. Li, K. Zhang, L. Fu, and B. A. Chin, "Novel magnetostrictive microcantilever and magnetostrictive nanobars for high performance biological detection," *Advances in Science and Technology*, vol. 54, pp. 19–28, 2008.

[6] L. Fustero, S. Li, K. Zhang, I.-H. Chen, V. A. Petrenko, and Z. Cheng, "Magnetostrictive Microcantilever as an Advanced Transducer for Biosensors," *Sensors*, vol. 7, no. 11, pp. 2929–2941, 2007.

[7] S. Li, L. Orona, Z. Li, and Z. Y. Cheng, "Biosensor based on magnetostrictive microcantilever," *Applied Physics Letters*, vol. 88, no. 7, pp. 7–10, 2006.

[8] S. W. Harun, K. S. Lim, C. K. Tio, K. Dimyati, and H. Ahmad, "Theoretical analysis and fabrication of tapered fiber," *Optik*, vol. 124, no. 6, pp. 538–543, 2013.

[9] D. Monzon-Hernandez, a. Martinez-Rios, I. Torres-Gomez, and G. Salceda-Delgado, "Compact optical fiber curvature sensor based on concatenating two tapers," *Optics Letters*, vol. 36, no. 22, p. 4380, 2011.

[10] W. Cui, J. Si, T. Chen, and X. Hou, "Compact bending sensor based on a fiber Bragg grating in an abrupt biconical taper," *Optics Express*, vol. 23, no. 9, p. 11031, 2015.

[11] S. K. Vashisth, "A review of microcantilever for sensing applications," *Journal of nanotechnology*, pp. 1–26, 2007.

[12] P. I. Oden, G. Y. Chen, R. A. Steele, R. J. Warmack, and T. Thundat, "Viscous drag measurements utilizing microfabricated cantilevers," *Applied Physics Letters*, vol. 68, no. 26, pp. 3814–3816, 1996.

[13] L. Zhao, L. Xu, G. Zhang, Z. Jiang, Y. Zhao, J. Wang, X. Wang, and Z. Liu, "In-situ measurement of fluid density rapidly using a vibrating piezoresistive microcantilever sensor without resonance occurring," *IEEE Sensors Journal*, vol. 14, no. 3, pp. 645–650, 2014.

[14] Q. Zhang, W. Ruan, H. Wang, Y. Zhou, Z. Wang, and L. Liu, "A self-bended piezoresistive microcantilever flow sensor for low flow rate measurement," *Sensors and Actuators, A: Physical*, vol. 158, no. 2, pp. 273–279, 2010.

[15] M. Godin, V. Tabard-Cossa, P. Grutter, and P. Williams, "Quantitative surface stress measurements using a microcantilever," *Applied Physics Letters*, vol. 79, no. 4, p. 551, 2001.

[16] J. R. Barnes, R. J. Stephenson, M. E. Welland, C. Gerber, and J. K. Gimzewski, "Photothermal spectroscopy with femtojoule sensitivity using a micromechanical device," 1994.

[17] Q. Zhu, W. Y. Shih, and W. H. Shih, "Enhanced detection resonance frequency shift of a piezoelectric microcantilever sensor by a DC bias electric field in humidity detection," 2009.

[18] C. De Angelis, V. Ferrari, D. Marioli, E. Sardini, M. Serpelloni, and A. Taroni, "Magnetically induced oscillations on a conductive cantilever for resonant microsensors," *Sensors and Actuators, A: Physical*, vol. 135, no. 1, pp. 197–202, 2007.

[19] D. Ma, J. L. Garrett, and J. N. Munday, "Quantitative measurement of radiation pressure on a microcantilever in ambient environment," *Applied Physics Letters*, vol. 106, no. 9, 2015.

[20] G. Meyer and N. M. Amer, "Novel optical approach to atomic force microscopy," *Applied Physics Letters*, vol. 53, no. 12, pp. 1045–1047, 1988.

[21] A. Kooser, R. L. Gunter, W. D. Delinger, T. L. Porter, and M. P. Eastman, "Gas sensing using embedded piezoresistive microcantilever sensors," *Sensors and Actuators, B: Chemical*, vol. 99, no. 2-3, pp. 474–479, 2004.

[22] M. K. Ghatkesar, E. Rakhmatullina, H. P. Lang, C. Gerber, M. Hegner, and T. Braun, "Multi-parameter microcantilever sensor for comprehensive characterization of Newtonian fluids," *Sensors and Actuators, B: Chemical*, vol. 135, no. 1, pp. 133–138, 2008.

[23] W. Shu, S. Laurenson, T. P. J. Knowles, P. Ko Ferrigno, and A. A. Seshia, "Highly specific label-free protein detection from lysed cells using internally referenced microcantilever sensors," *Biosensors and Bioelectronics*, vol. 24, no. 2, pp. 233–237, 2008.

[24] G. Wu, R. H. Datar, K. M. Hansen, T. Thundat, R. J. Cote, and A. Majumdar, "Bioassay of prostate-specific antigen (PSA) using microcantilevers.," *Nature Biotechnology*, vol. 19, no. September, pp. 856–860, 2001.

[25] R. Datar, A. Passian, R. Desikan, and T. Thundat, "Microcantilever biosensors," in *Proceedings of IEEE Sensors*, p. 5, 2007.

[26] H. Etayash, K. Jiang, S. Azmi, T. Thundat, and K. Kaur, "Real-time Detection of Breast Cancer Cells Using Peptide-functionalized Microcantilever Arrays," *Scientific Reports*, no. August, pp. 1–13, 2015.

[27] R. L. Gunter, W. G. Delinger, K. Manygoats, A. Kooser, and T. L. Porter, "Viral detection using an embedded piezoresistive microcantilever sensor," *Sensors and Actuators, A: Physical*, vol. 107, no. 3, pp. 219–224, 2003.

[28] B. H. Cha, S.-M. Lee, J. C. Park, K. S. Hwang, S. K. Kim, Y.-S. Lee, B.-K. Ju, and T. S. Kim, "Detection of Hepatitis B Virus (HBV) DNA at femtomolar concentrations using a silica nanoparticle-enhanced microcantilever sensor," *Biosensors and Bioelectronics*, vol. 25, no. 1, pp. 130–135, 2009.

[29] H. H. Kim, H. J. Jeon, H. K. Cho, J. H. Cheong, H. S. Moon, and J. S. Go, "Highly sensitive microcantilever biosensors with enhanced sensitivity for detection of human papilloma virus infection," *Sensors and Actuators, B: Chemical*, vol. 221, pp. 1372–1383, 2015.

[30] T. Itoh and T. Suga, "Force sensing microcantilever using sputtered zinc oxide thin film," *Applied Physics Letters*, vol. 64, no. 1, pp. 37–39, 1994.

[31] M. Álvarez and J. Tamayo, "Optical sequential readout of microcantilever arrays for biological detection," *Sensors and Actuators, B: Chemical*, vol. 106, no. 2, pp. 687–690, 2005.

[32] D. Rugar, H. J. Mamin, and P. Guethner, "Improved fiber-optic interferometer for atomic force microscopy," *Applied Physics Letters*, vol. 55, no. 25, pp. 2588–2590, 1989.

[33] R. C. O'Handley, *Modern Magnetic Materials: Principles and Applications*. 2000.

[34] A. Bieńkowski, "Magnetoelastic Villari effect in Mn-Zn ferrites," *Journal of Magnetism and Magnetic Materials*, vol. 215, no. 1, pp. 231–233, 2000.

[35] H. Kwun and K. Bartels, "Magnetostrictive sensor technology and its applications," *Ultrasonics*, vol. 36, no. 1, pp. 171–178, 1998.

[36] C. D. G. Cullity, B. D., *Introduction to Magnetic Materials*. 111 River Street, Hoboken, NJ: John Wiley & Sons, Inc., 1972.

[37] D. Hunter, W. Osborn, K. Wang, N. Kazantseva, J. Hattrick-Simpers, R. Suchoski, R. Takahashi, M. L. Young, A. Mehta, L. a. Bendersky, S. E. Lofland, M. Wuttig, and I. Takeuchi, "Giant magnetostriction in annealed Co1âxFex thin-films," *Nature Communications*, vol. 2, no. May, p. 518, 2011.

[38] A. E. Clark, J. B. Restorff, M. Wun-Fogle, T. A. Lograsso, and D. L. Schlagel, "Magnetostrictive properties of body-centered cubic Fe-Ga and Fe-Ga-Al alloys," in *IEEE Transactions on Magnetics*, vol. 36, pp. 3238–3240, 2000.

[39] F. Alam, M. M. Kamal, and M. A. Asgar, "Study of magnetostriction in iron and cobalt based amorphous magnetic materials," *Proceedings of 4th International Conference on Electrical and Computer Engineering, ICECE 2006*, no. December, pp. 366–369, 2007.

[40] M. D. Cooke, L.-c. Wang, R. Watts, R. Zuberek, and G. Heydon, "The effect of thermal treatment , composition and substrate on the texture and magnetic properties of FeCo thin films," vol. 1450, 2000.

[41] R. Zhang, X. Zhang, D. Meiser, and H. Giessen, "Mode and group velocity dispersion evolution in the tapered region of a single-mode tapered fiber.," *Optics express*, vol. 12, no. 24, pp. 5840–9, 2004.

[42] B. S. Kawasaki, K. O. Hill, and R. G. Lamont, "Biconical-taper single-mode fiber coupler.," *Optics letters*, vol. 6, no. 7, pp. 327–8, 1981.

[43] L. Lv, S. Wang, L. Jiang, F. Zhang, Z. Cao, P. Wang, Y. Jiang, and Y. Lu, "Simultaneous measurement of strain and temperature by two peanut tapers with embedded fiber Bragg grating," *Applied Optics*, vol. 54, no. 36, p. 10678, 2015.

[44] J. F. Ding, A. P. Zhang, L. Y. Shao, J. H. Yan, and S. He, "Fiber-taper seeded long-period grating pair as a highly sensitive refractive-index sensor," *IEEE Photonics Technology Letters*, vol. 17, no. 6, pp. 1247–1249, 2005.

[45] F. Xu, C. Li, D. Ren, L. Lu, W. Lv, F. Feng, and B. Yu, "Temperature-insensitive Mach-Zehnder interferometric strain sensor based on concatenating two waist-enlarged fiber tapers," *Chinese Optics Letters*, vol. 10, no. 7, p. 70603, 2012.

[46] C. Wuttke, M. Becker, S. Brückner, M. Rothhardt, and A. Rauschenbeutel, "Nanofiber Fabry-Perot microresonator for nonlinear optics and cavity quantum electrodynamics.," *Optics letters*, vol. 37, no. 11, pp. 1949–1951, 2012.

[47] M. Pospisilova, G. Kuncova, and J. Trogl, "Fiber-optic chemical sensors and fiber-optic bio-sensors," *Sensors (Switzerland)*, vol. 15, no. 10, pp. 25208–25259, 2015.

[48] P. J. Kelly and R. D. Arnell, "Magnetron sputtering: a review of recent developments and applications," *Vacuum*, vol. 56, no. 3, pp. 159–172, 2000.

[49] J. E. Crowell, "Chemical methods of thin film deposition: Chemical vapor deposition, atomic layer deposition, and related technologies," *Journal of Vacuum Science & Technology A: Vacuum, Surfaces, and Films*, vol. 21, no. 2003, p. S88, 2003.

[50] H. Jansen, H. Gardeniers, and M. D. Boer, "A survey on the reactive ion etching of silicon in microtechnology," *J. Micromech. Microeng.*, vol. 6, pp. 14–28, 1996.

[51] B. A. Movchan, "Discrete nanosized metallic coatings produced by EB-PVD," *Surface Engineering*, vol. 32, no. 4, pp. 258–266, 2016.

[52] K. Vernon-Parry, "Scanning electron microscopy: an introduction," *III-Vs Review*, vol. 13, no. 4, pp. 40–44, 2000.

[53] R. Groessinger, "Characterization of Hard Magnetic Materials," *Journal of Electrical Engineering*, vol. 59, no. 7, pp. 15–20, 2008.

[54] J. Villatoro, D. Monzón-Hernández, and E. Mejía, "Fabrication and modeling of uniform-waist single-mode tapered optical fiber sensors.," *Applied optics*, vol. 42, no. 13, pp. 2278–2283, 2003.

[55] J. Shi, S. Xiao, L. Yi, and M. Bi, "A sensitivity-enhanced refractive index sensor using a single-mode thin-core fiber incorporating an abrupt taper," *Sensors*, vol. 12, no. 4, pp. 4697–4705, 2012.

[56] H. J. Kbashi, "Fabrication of Submicron-Diameter and Taper Fibers Using Chemical Etching," *Journal of Materials Science and Technology*, vol. 28, no. 4, pp. 308–312, 2012.

[57] F. Bayle and J.-P. Meunier, "Efficient fabrication of fused-fiber biconical taper structures by a scanned CO2 laser beam technique.," *Applied optics*, vol. 44, no. 30, pp. 6402–11, 2005.

[58] T. E. Dimmick, G. Kakarantzas, T. A. Birks, and P. S. J. Russell, "Carbon dioxide laser fabrication of fused-fiber couplers and tapers," *Applied Optics*, vol. 38, no. 33, p. 6845, 1999.

[59] Y. Zhang, A. Dhawan, and T. Vo-Dinh, "Design and Fabrication of Fiber-Optic Nanoprobes for Optical Sensing," *Nanoscale Research Letters*, vol. 6, no. 1, pp. 1–6, 2011.

[60] M. Rajibul Islam, M. Mahmood Ali, M. H. Lai, K. S. Lim, and H. Ahmad, "Chronology of fabry-perot interferometer fiber-optic sensors and their applications: A review," *Sensors (Switzerland)*, vol. 14, no. 4, pp. 7451–7488, 2014.

[61] J. Schrauwen, D. Van Thourhout, and R. Baets, "Focused-ion-beam fabricated vertical fiber couplers on silicon-on-insulator waveguides," *Applied Physics Letters*, vol. 89, no. 14, pp. 2004–2007, 2006.

[62] R. M. André, S. Pevec, M. Becker, J. Dellith, M. Rothhardt, M. B. Marques, D. Donlagic, H. Bartelt, and O. Frazão, "Focused ion beam post-processing of optical fiber Fabry-Perot cavities for sensing applications.," *Optics Express*, vol. 22, no. 11, pp. 13102–8, 2014.

[63] L. Bian, Y. Wen, P. Li, Y. Wu, X. Zhang, and M. Li, "Magnetostrictive stress induced frequency shift in resonator for magnetic field sensor," *Sensors and Actuators, A: Physical*, vol. 247, pp. 453–458, 2016.

[64] M. Hirano, K. Harada, Y. Ishihara, T. Todaka, and K. Fujiwara, "A Study on Measurement of Magnetostriction of Silicon Steel Sheet," vol. 255, pp. 43–46, 2003.

[65] G. Berkovic and E. Shafir, "Optical methods for distance and displacement measurements," *Advances in Optics and Photonics*, vol. 4, no. 4, p. 441, 2012.

[66] L. M. Manojlović, "Resolution limit of the quadrant photodetector," *Optik - International Journal for Light and Electron Optics*, vol. 127, no. 19, pp. 7631–7634, 2016.

[67] M. S. Cheri, H. Latifi, F. B. A. Aghbolagh, O. R. R. Naeini, M. Taghavi, and M. Ghaderi, "Fabrication, characterization, and simulation of a cantilever-based airflow sensor integrated with optical fiber," *Applied optics*, vol. 52, no. 14, pp. 3420–7, 2013.

[68] W. Gong, H. Li, Z. Zhao, and J. Chen, "Ultrafine particles of Fe, Co, and Ni ferromagnetic metals," *Journal of Applied Physics*, vol. 69, no. 8, pp. 5119–5121, 1991.

[69] K. H. Na, Y. S. Kim, and C. J. Kang, "Fabrication of piezoresistive microcantilever using surface micromachining technique for biosensors," in *Ultramicroscopy*, vol. 105, pp. 223–227, 2005.

[70] L. A. Pinnaduwage, J. E. Hawk, V. Boiadjiev, D. Yi, and T. Thundat, "Use of microcantilevers for the monitoring of molecular binding to self-assembled monolayers," *Langmuir*, vol. 19, no. 19, pp. 7841–7844, 2003.

[71] S. C. Warren-Smith, R. M. André, C. Perrella, J. Dellith, M. Rothhardt, and H. Bartelt, "Direct core structuring of microstructured optical fibers using focused ion beam milling," *Optics Express*, vol. 24, no. 1, 2016.

[72] R. M. André, S. C. Warren-Smith, M. Becker, J. Dellith, M. Rothhardt, M. I. Zibaii, H. Latifi, M. B. Marques, H. Bartelt, and O. Frazão, "Simultaneous measurement of temperature and refractive index using focused ion beam milled Fabry-Perot cavities in optical fiber micro-tips," *Optics Express*, vol. 24, no. 13, p. 14053, 2016.